

EXCITON-TRION-POLARITONS IN
TWO-DIMENSIONAL TRANSITION-METAL
DICALCOGENIDES

A Dissertation

Presented to the Faculty of the Graduate School
of Cornell University

in Partial Fulfillment of the Requirements for the Degree of
Doctor of Philosophy

by

Okan Koksal

August 1, 2021

© 2021 Okan Koksall
ALL RIGHTS RESERVED

EXCITON-TRION-POLARITONS IN TWO-DIMENSIONAL TRANSITION-METAL DICHALCOGENIDES

Okan Koksal, Ph.D.

Cornell University 2021

This dissertation covers a series of experiments that realized, investigated, and controlled exciton-trion-polaritons in transition-metal dichalcogenides (TMDs). First, theoretical and experimental research that led to the established understanding of trions are reviewed. Then, recent theoretical developments that led to a complete reimagining of excitons, trions, and their interactions with photons is discussed. With the theoretical background established, detailed measurements of optical conductivity of TMD MoSe₂ are combined with quantitative analysis to determine the nature of strong Coulomb interactions between excitons and bound trions in TMDs. Then, design and simulations of, and measurements on a hybrid photonic-crystal-TMD structure is discussed whereupon remarkable agreement between experiment and theory evidences the existence of coherent exciton-trion-polariton formation. Initial experimental forays into electronic control of the optical properties of this polariton system is then reviewed. In the final chapter of this dissertation, a non-exhaustive investigation of potential device applications based on the understanding of exciton-trion-polaritons is conducted.

BIOGRAPHICAL SKETCH

Okan Köksal was born on March 9, 1992 to Adnan Köksal, a Professor of Electrical Engineering in Hacettepe University, Turkey and Gülser Köksal, a Professor in Industrial Engineering in Middle East Technical University (METU), Turkey. Okan was born in the United States, but his parents moved back to Turkey when he was one year old. They returned to the US briefly when he was four. He has fond, albeit sporadic memories of that second time he spent in the US. After that time, Okan grew up in the METU campus of Ankara, Turkey. Between a mixture of the delicious smell of coffee at home he was not allowed to drink as a child, and the collegial atmosphere of the university he grew up in, Okan was a bookish child. He did not find his bookishness conflicting with the martial arts lessons he attended for the majority of his childhood; being a fond admirer of the philosopher-king archetype. He attended elementary in ODTÜ Koleji Geliştirme Vakfı Özel İlköğretim Okulu, a private school in METU campus grounds. He received a love of academic pursuit in these days, finding like-minded friends who enjoyed deep, philosophical discussions as much as he did. He then attended the Ankara Atatürk Anadolu Lisesi, one of the top high schools in Ankara and the nation.

He thrived in the competitive atmosphere there, and perhaps a bit too much: since he surprised himself by gaining admission to University of Illinois at Urbana-Champaign (UIUC) while also studying for the Turkish university entrance exams. Thanks to his parents' encouragement, guidance and help, he took the leap to return to his land of birth as an Electrical Engineering undergraduate student. While in UIUC, he obtained a Mathematics Minor with an eye on the area of Signal Processing. In his Senior year, his career plans changed abruptly; he found that he absolutely loved the courses he took on classical op-

tics and lasers. With a Mathematics Minor at his belt, he applied for graduate school in Cornell, intending to join Professor Farhan Rana.

He was beyond excited when he was accepted. Okan's first few years in Cornell were challenging, but extremely rewarding. He developed a newfound love towards solid-state physics. The more he understood how experimental science and research worked, the more he enjoyed it. In 2017, he received a Best Poster award over his presentation given in his Alma Mater, UIUC. He still remembers that Prof. Rana asked him if he knew about trions in his first visit to Cornell. He committed to the problem of trions after 2018, following a fruitful year of investigations into defects of Ga_2O_3 . This project has expanded Okan's horizons on conducting research, allowed him to establish professional, collaborative relations with his peers, and made him truly enjoy precise agreement between measurement and theory. He is excited about continuing his work, and pursuing new topics of condensed matter research as a postdoctorate researcher.

Dedicated to the relentless pursuers of knowledge; the people who love them,
and are loved by them. Because life is too precious a gift to not love what one
does, or who one is.

ACKNOWLEDGEMENTS

One of the most beautiful and poignant moments in a student's is immediately before change. Learning how to be a researcher is a somewhat hectic chase of putting out one small fire after another; wherein it is easy to miss many a great moment one gets to share with friends, family, peers, competitors, staff and faculty.

Perhaps one of the greatest advantages of writing a PhD thesis, especially in today's hyper-connected, overly rushed, and over-informed world, is that the time it takes to write a thesis allows for meditations on the many years that passed in the pursuit that is called a PhD.

I am lucky to have had that brief moment of respite in order to think about all of whom I have to thank for having brought me to this point. What follows is my attempt at recording these meditations.

I owe much gratitude to Cornell staff, without whose diligence and patience I would be lost during many a task. Scott Coldren's boundless knowledge of administrative processes, Patty Gonyea's help in building affairs which included an entire laboratory move, Eric Smith's willingness to share his boundless experience in cryogen science, and CNF staff's persistent availability in sharing their immense combined expertise in nanofabrication all proved deeply valuable to me during my time as a PhD student. I am also very lucky to have known the Mattin's staff. Sharon and Tamrie brightened my day with a smile after many an early morning, along with my usual muffin and coffee combo.

I was mentored by two excellent former graduate students in our group: Haining Wang and Jared Strait. In the many days I shadowed Haining, an arrangement he patiently accomodated, the skills I developed in optical spectroscopy and nanofabrication served as the foundation of much of the work I

did in pursuit of this Thesis. Besides instilling in me a deep passion for measurement science and spectroscopy, as well as a passion for quantitative accuracy in measurements; Jared's mentoring oversaw my first forays into experimental physics. Also, I will forever be grateful for Jared's kind invitation to visit the Gaithersburg campus of the National Institute of Standards and Technology early on in my graduate career. This visit introduced me to the field of metrology that I now deeply resonate with.

Besides Jared and Haining, Long Ju has been a delight to have as a lab-mate. His relentless drive for precision and quantitative accuracy in experiments has been a benchmark against which I constantly weigh my own work. Long was also a great friend to have in and out of the lab. I wish him continued success in his professorship at Massachusetts Institute of Technology.

One amazing aspect of Cornell is how it brings together so many excellent lecturers into one campus. Though I took many amazing courses here in Cornell, I feel especially thankful to a few for teaching me so much: Prof. Frank Wise on nonlinear optics, Prof. Debdeep Jena on solid-state physics and quantum transport, Prof. Francesco Monticone on connections between classical electrodynamics and solid-state physics.

I was extremely fortunate have met the three junior graduate students who joined our group; just as I was eager to pass on the knowledge I accumulated from Jared, Haining, and Long. It is thanks to the patience and constructiveness with which Joongwon Lee accepted my mentorship that gave me the chance to express my thoughts more clearly. I owe no small thanks to Arjan Singh, whose rapid adaptation into my old project allowed me to concentrate my attention to the work on this Thesis. Besides, Arjan is a voracious reader of textbooks and literature, and is always willing to entertain lengthy discussions about either.

Yifei Geng has also been a rapid and passionate learner of both theory and experimental physics. His really tough questions are always a joy to think about! All three are excellent researchers already who I know will continue to be very successful. Besides being excellent coworkers, they were all great friends; I will miss them.

As I was engaged in graduate research, I found little time to cultivate new friendships outside the office. I did meet some great people, and I hope that our friendships were as meaningful to them as it was to me. I therefore found the brief time I could spend with my close friends, all of whom are abroad, precious. Burak Yürekli, Tolga Yaman, and Toros Arıkan have all been amazing and steadfast friends; this, despite the geographical barriers that seem ever mounting in today's stricken World. I also owe a special thanks to Jasmine, with whom I found capacity within to do much more. I hope life brings her happiness.

Of course, I owe so much to my parents, Gülser and Adnan. They were always there for me when I needed someone to talk to; listening patiently and caringly no matter how much frustration about graduate research I conveyed. It is my parents who instilled in me a deep love for academic thinking; and whose unwavering support gave me the willingness to take on a project that appeared so difficult and yet was so rewarding in the end.

Finally, it is to my advisor, Professor Farhan Rana that I owe heartfelt gratitude. My academic formation owes a great deal to the amazing courses he prepared and taught on solid state physics, quantum optics, semiconductor optics, and electromagnetics. He has patiently allowed me to take risks and to establish my own identity as an academic researcher; a rare privilege in today's extremely demanding research atmosphere. In the pursuit of intellectual independence, I hit many a stumbling block that Prof. Rana's sound advice helped me recover

from. He has been, and continues to be a role model for me. In addition to all of this, Prof. Rana embodies the Cornell spirit fully. It is through the example he set that I now aspire to enter every day in order to become more learned, and so depart the day to become more useful to my country and to humankind.

TABLE OF CONTENTS

| | |
|--|-----------|
| Biographical Sketch | iii |
| Dedication | v |
| Acknowledgements | vi |
| Table of Contents | x |
| List of Tables | xii |
| List of Figures | xiii |
| | |
| 1 An Introduction to Trions and the Trion-Photon Interaction Problem | 1 |
| 1.0.1 Theory of Trions as 3-body, Fermionic States | 2 |
| 1.0.2 Fermi-Polarons Instead of Trions? | 4 |
| 1.1 A Novel Theory of Trions as 4-Body, Bosonic States | 6 |
| 1.1.1 Exciton-Trion-Polaritons | 8 |
| | |
| 2 Optical Conductivity of Monolayer Molybdenum Diselenide | 13 |
| 2.1 Measurement of Optical Conductivity of Monolayer MoSe ₂ | 14 |
| 2.1.1 Fabrication and Deterministic Dry-Transfer of 2D-Layered Materials | 14 |
| 2.1.2 Experimental Setup | 21 |
| 2.2 Measurement, Results, and Analysis | 24 |
| | |
| 3 Realization of Exciton-Trion-Polaritons in Hybrid Photonic-2D Material Systems | 30 |
| 3.1 One-Dimensional Photonic Crystals as a Means of Inducing Strong Optical Coupling | 30 |
| 3.1.1 Design of 1D Photonic Crystals | 31 |
| 3.1.2 Fabrication of 1D Photonic Crystals | 33 |
| 3.2 Experimental Setup for Momentum-Space Dispersion Measure- ments | 34 |
| 3.2.1 Measurement and Analysis of Bare Waveguide Mode Dispersion | 36 |
| 3.3 Exciton-Trion-Polaritons in Hybrid Photonic-2D Material Systems | 37 |
| 3.3.1 In-Situ Optical Characterization of Monolayer MoSe ₂ Op- tical Conductivity | 38 |
| 3.3.2 Dispersion of Exciton-Trion-Polaritons | 40 |
| 3.3.3 Dispersion of Exciton-Trion-Polaritons via Photolumines- cence | 41 |
| | |
| 4 Controlling Exciton-Trion-Polariton Dispersion by Tuning Carrier Density | 50 |
| 4.1 Fabrication Considerations to Realize Simultaneous, Strong Op- tical and Coulomb Coupling in Exciton-Trion-Polaritons | 52 |
| 4.1.1 Photonic Crystal Fabrication. | 52 |

| | | |
|----------|--|-----------|
| 4.1.2 | hBN Encapsulation of Monolayer MoSe ₂ | 54 |
| 4.2 | Electrical Control of Exciton-Trion-Polariton Dispersion | 56 |
| 4.2.1 | Discussion on Device Ideality and Exciton Localization | 59 |
| 5 | Discussion and Outlook | 63 |
| 5.1 | Potential Device Applications of Exciton-Trion-Polaritons | 63 |
| 5.1.1 | Low Power Optoelectronic, or All-Optical Modulators | 63 |
| 5.1.2 | Exciton-Trion-Polariton Metasurfaces | 65 |
| 5.2 | Conclusion | 68 |
| A | Cryogenic Confocal Microscope Alignment Details | 69 |
| A.1 | Aligning the Monochromator and CCD | 69 |
| A.2 | Mapping Horizontal Pixels to Wavelength | 71 |
| A.3 | Mapping Vertical Pixels to Photon Momentum | 73 |
| A.4 | Liquid Helium Transfer Procedure | 76 |
| B | Finite-Difference Frequency-Domain Measurements | 79 |
| C | Potential Methods to Improve Exciton-Trion-Polariton Device Quality | 81 |
| C.1 | Disorder in 2D Layered Materials | 81 |
| C.2 | Contamination-Free Dry Transfer Using Polymer-Based Stamps | 82 |
| D | Recent Results Similar to that of Exciton-Trion-Polaritons | 84 |
| | Bibliography | 85 |

LIST OF TABLES

| | | |
|-----|---|----|
| 2.1 | Photolithography of Metal Contacts | 20 |
| 3.1 | PMMA-Based Grating Fabrication Recipe | 33 |
| 4.1 | ZEP520A-Based Grating Fabrication Recipe | 54 |
| 4.2 | Comparison of Extracted and Calculated Carrier Densities of Exciton-Trion-Polariton Device | 61 |

LIST OF FIGURES

| | | |
|-----|---|----|
| 1.1 | Real-space and momentum space representations of excitons and trions in an electron-doped TMD monolayer, according to the three-particle model of trions. a. A bound state formed between a photo-excited conduction band electron, valence band hole pair results in an exciton state. In momentum space, this electron-hole pair, possessing a finite momentum, is shown by the red ellipse. K and K' valleys correspond to the two spin-valley configurations in TMDs. The exciton state can also be formed in the K' valley. Photon emission conserves linear and angular momentum b. The trion state, constructed as a three-particle state comprised of two conduction band electrons, and one valence band hole. The extra electron belongs to the opposite K valley. To conserve total momentum upon photo-emission, the electron in the opposite K' valley has to scatter above the Fermi level. | 3 |
| 1.2 | Real-space representations of attractive and repulsive Fermi-polaron states. a. Attractive Fermi-polaron. The electron cloud (shown in red) surrounding the exciton is brought closer to the exciton due to Coulomb interactions. b. Repulsive Fermi-polaron. The electron cloud (shown in red) surrounding the exciton is pushed away further from the exciton due to Coulomb interactions. | 5 |
| 1.3 | Two- and four-particle bound states and their interactions according to [22]. a. Exciton state. The interband electron-hole pair is shaded in orange. b. Bound trion state. An interband electron-hole pair combined with an intraband electron-hole pair that forms the state is shaded in orange. Here, the hole shown in green is the conduction band hole, which is also referred to as the exchange correlation hole. For the bound trion state to be correctly analyzed, Coulomb interactions between the exchange correlation hole and the other three particles need to be considered. c. Exciton-trion superposition states due to Coulomb coupling. Strength of the Coulomb coupling depends on n_e , the background carrier density. Eigenstates of the system, denoted as a and b here, are coherent exciton-trion superposition states. . | 11 |

| | | |
|-----|--|----|
| 1.4 | Exciton-trion-polaritons in 2D semiconductors. a. A complete model of coupled oscillator interactions that describe exciton-trion-polaritons. The optical coupling between ground state and exciton is then followed by Coulomb coupling between excitons, and bound or unbound trions. A coherent superposition state can form between excitons, bound trions, and photons. Unbound trion states form a continuum, which is one of the mechanisms that reduces the lifetime of these coherent states [57]. b. A description of why the three-particle trion model does not predict coherent trion-polaritons. When a trion of certain momentum emits a photon, the second CB electron ends up above the Fermi level. Meanwhile, the new CB electron taken from the Fermi sea lies beneath the Fermi level; necessitating a change in trion momentum after the photon is reabsorbed. Coherence of trion-photon interactions are quickly lost. c. How a coherent exciton-trion-polariton state is formed. Due to Coulomb interactions, the trion couples to an exciton state. This exciton state emits, and reabsorbs a photon, and then couples back to the first trion state. Thus, the trion-photon interaction, while indirect, is entirely coherent. | 12 |
| 2.1 | Encapsulated monolayer MoSe ₂ capacitor device used in carrier-density-dependent optical conductivity measurements. a. Side-view of the device, along with the measurement scheme. The monolayer is directly exfoliated on the SiO ₂ layer, and is encapsulated by hBN. Ti/Au contacts are deposited on the exposed portion of the monolayer. Normalized reflectivity measurements are done by a confocal reflectance measurement on the sample, and normalized by a confocal reflectance measurement on the hBN encapsulated oxide substrate. The ratio of these measurements is then compared to the calculated transmission spectrum. b. Top-down view of the sample. | 15 |
| 2.2 | Summary of dry transfer step preparation. a. Nitto-Denko tape is cut into strips, and edges are folded. b. A small section is cut from a large, shiny, and recently-opened flake of bulk, flux-zone-grown MoSe ₂ . c. The tape is populated until a smooth, shiny film covers the whole tape. d. PDMS stamps are placed on high quality microscope slides. Slides are rinsed to remove dust specks that can come between PDMS and glass. PDMS films should be bubble and wrinkle-free for best device yield. e. PDMS stamps are flipped and placed over the populated blue tape. Mild pressure is applied to push air out of contact area. After one minute, stamps are carefully peeled from tape. | 17 |

| | | |
|-----|---|----|
| 2.3 | 2D transfer process and setup. a. Desired flakes on the device are approximately marked in two orthogonal axes using a silver marker. A 1 mm ² area around the flake is then cut. b. A photograph of the 2D transfer setup. While oxygen damage is well-studied in literature, this transfer setup did not employ a glove-box as devices were fabricated within 24 hours of the flakes being exfoliated. c. Close-up image of the microscope, the transfer slide, sample, and hot plate the sample is placed on. d. A depiction of how the PDMS film transfers the flake on the substrate. The three stages of how the PDMS is shaped is approximate, but the curvature of PDMS could be easily determined by interference and color contrast on the microscope image. All dry-transfer processes took place at 46 °C. | 18 |
| 2.4 | Diagram and photographs of the optical spectroscopy measurement setup. a. The microscope section depicts the white light, shown in red, being collimated out of the multimode fiber and refocused onto the cryostat. The reflected light passes through the spatial filter, which accepts only collimated light, and enters the spectrometer. b. Photos of the setup. Clockwise from top left: The cryostat cold finger chip socket. Packaged devices mate into this socket, and can thus be electrically controlled via a bias circuit (not shown) outside the cryostat; He flow and temperature control electronics for the cryostat; the setup at work; the x-y-z stage mount for the cryostat. The cryostat is held by numerous clamps, which minimizes vibrations. To further minimize vibrations, the pressure points between clamps and the cryostat are separated by a soft tissue, which reduces pressure and increases force on the cryostat. The clamps are held by a vibration-dampening post. Furthermore, the cryostat is supported from below by a metal post with another tissue between the cryostat and the metal post. Care was taken to ensure the center of gravity lies within the transfer stage. The post was placed towards the fixed point of the 2D transfer stage to ensure minimal vibrations. | 23 |

| | | |
|-----|---|----|
| 2.5 | <p>Normalized reflectivity, optical conductivity fits, and linear dependence of Fermi level and carrier density. a. Evolution of the normalized reflectivity as bias voltage is decreased from +2V to -34V (carrier density changed from intrinsic levels to large n-doping). The large resonance at 1.65 eV disappears as carrier density is increased. Conversely, a second resonance, unseen at intrinsic carrier densities, emerges as carrier density increases; eventually becoming larger than the resonance at 1.65 eV. b. Fits of two select carrier densities using the transfer-matrix model based on optical conductivity spectra of [22]. In order to approximately fit the feature at 1.8 eV, possibly due to B-exciton absorption, two phenomenological resonances were introduced to mimic B-exciton, and bandgap absorption. These did not affect the reflectivity contrast at 1.65 eV or below greatly; so did not change the physics being discussed. c. Using best fits, examples of which were shown in (b), dependence of splitting energy between upper and lower exciton-trion resonances, and gate voltage was measured. The device is in accumulation mode, so gate voltage and carrier density are linearly proportional. Since carrier density and Fermi level are proportional, the measured peak splitting is approximately linear with Fermi level, as predicted by various theoretical works. [60, 13, 22].</p> | 25 |
| 3.1 | <p>Hybrid photonic crystal-monolayer MoSe₂ device used to realize exciton-trion-polariton dispersion. a. 3D diagram of the device. For an incoming plane wave of momentum \vec{k}, the TE-polarization shown in blue couples to the PC modes. Due to the large photonic crystal momentum, the TM-modes are almost along the y axis, so any optical excitation in the experiment discussed in this chapter could excite TM-modes. b. Band structure of the photonic crystal across \vec{k}_x and \vec{k}_z directions for TE- and TM-modes. The heavier blue band is used for exciton-trion-polariton dispersion measurements. The approximate energy of the lower exciton-trion resonance is indicated by the large red arrow. c. Normalized electric field intensity distribution across one period of the photonic crystal at $\vec{k}_z = \vec{k}_x = 0$ for the highlighted TE-mode. Imperfect, but decent mode overlap of the waveguide mode with the monolayer is found.</p> | 43 |

| | | |
|-----|---|----|
| 3.2 | <p>a. Photo of fabricated grating structure, due to diffraction, semi-circles brightly colored in green and other hues can be seen. These sharp colors could be used as a quick sanity-check of grating quality before quantitative measurements begin. b. Microscope image of device used in measurements discussed in this Chapter. The blue areas are that of the grating, and is caused by the cross-polarization technique used in obtaining the microscope image. The light gray area in the center is the monolayer MoSe₂ flake. It can be seen that large cracks, and other disorder is present. However, large areas of the sample were not affected (at scales resolvable by visible wavelengths) by disorder. An astute observer might notice that the top of the flake is darker than the center. This is believed to be due to carrier density variations of the monolayer flake. However, short of a large-area, broadband, in-situ spectroscopy measurement, this belief could not be verified.</p> | 44 |
| 3.3 | <p>Setup and measurement summary a. Diagram of the setup looking from the top, and head-on. 532 nm laser used for alignment and PL not shown. White light exits the multimode fiber, is collimated, color-filtered, polarized, and sent into the microscope. The frontal view of the objective shows that the collimated white light diameter is slightly larger than the back-focal plane diameter (D), ensuring the full numerical aperture of the objective is utilized. The frontal view of the pinhole shows how the pinhole spatially filters a small diameter (P) of white light. P was magnified to $\sim 10\mu\text{m}$ on the image plane. Head-on view of the slit shows how only the immediate vicinity of $k_x = 0$ is selected for dispersion measurements. The diameter of this slit simultaneously sets the frequency and momentum resolution of the setup. Appropriate choice of collimator and high-resolution objective played a significant role in ensuring high-quality, artifact free dispersion measurements. b. Three different measurements whose effective collection area are highlighted in pink are shown. (1), (2), and (3) correspond to the bare waveguide, loaded waveguide, and unpatterned substrate, respectively. All measurements in this Chapter, unless states otherwise, were done at 20 K.</p> | 45 |

| | | |
|-----|---|----|
| 3.4 | Unloaded waveguide dispersion. a. Right-hand side: Unloaded waveguide dispersion measured via normalized reflectivity. Left-hand side: FDFD Fit to the measured dispersion. FDFD was normalized in the same manner as the measurements. Remarkable agreement between theory and measurement can be seen. b. Scheme to obtain normalized reflectivity. Numbered pink areas denote the locations on the sample where each measurement was taken. Unloaded waveguide dispersion measurements normalized 1 by 3. Electric field, and dispersion measurement direction were both along the z-axis. | 46 |
| 3.5 | Determining in-situ optical conductivity of the monolayer MoSe ₂ flake. a. Top; optical conductivity model generated from [22]. Bottom; measured normalized reflectivity spectra and theory fits showing strong agreement. Measurements were obtained via dispersive measurements, and only the zero-momentum area was averaged. FDFD fits were normalized and momentum-space filtered in exactly the same fashion as the measurements. FDFD fits used the optical conductivity shown on the top side. b. Measurement scheme. Area 2 was normalized by Area 1. Dispersion measurements were along z-axis, but only a small region around zero-momentum was averaged to generate curves in (a). Electric field of incoming white light was polarized along the x-direction. This polarization strongly couples to neither TE-, nor TM-polarized PC modes. | 47 |
| 3.6 | Exciton-trion-polariton dispersion via normalized reflectivity. a. Comparison of measured (right-hand side) and theoretical (left-hand side) dispersions of exciton-trion-polaritons. Remarkable quantitative agreement between theory and measurements can be seen. Both results have three Rabi-split positive-mass polariton bands; denoted lower (LP), middle (MP), and upper (UP) polariton bands. Slight quantitative disagreements between measured, and theory dispersions is attributed to disorder in the photonic crystal structure b. Measurement scheme for normalized reflectivity. Numbered pink areas denote the locations on the sample where each measurement was taken. Unloaded waveguide dispersion measurements normalized 1 by 3. Electric field, and dispersion measurement direction were both along the z-axis. | 48 |

| | | |
|-----|---|----|
| 3.7 | <p>Exciton-trion-polariton dispersion via photoluminescence. a. Comparison of measurement (right-hand side) and theory (left-hand side). Theory curves were generated by photon density of states, calculated via the Green's function method. Reasonable agreement can be seen between the two curves; and disagreements are elaborated on (c) b. Measurement scheme. A 532 nm, continuous-wave laser was used to photo-excite carriers, resulting in PL emission. Dispersion of the PL was obtained along the z-axis. PL emission was linearly polarized along the z-axis. Dispersion was seen not to depend strongly on pump polarization, which was always linear. c. Temperature-dependence of PL from the MoSe₂ monolayer, in the weak-optical-coupling regime. A redshift of the upper and lower exciton-trion resonances can be seen, while the splitting energy between the bands were not found to depend strongly on temperature. This redshift partly explains why the LP band is significantly redshifted; sample heating due to the relatively high fluences used in the PL measurement tuned the lower E-T superposition state closer to the bottom of the PC mode, increasing the LP-MP splitting. The upper polariton band seen in theory curves is almost missing from measurements. This could be explained by the lower E-T having much larger PL emission spectral weight due to the incoherent relaxation from the upper E-T resonance to the lower one before photoemission [57].</p> | 49 |
| 4.1 | <p>Simulated carrier-density control of exciton-trion-polaritons in an idealized, but practically-attainable device. a. Intrinsic, b. Small, and c. Large n-doping of the sample. For each curve, the upper and lower exciton-trion (E-T) superposition states are shown by dashed green lines. As carrier density is increased, the LP-MP polariton bandgap opens around the lower E-T superposition state, which is redshifted due to increased Coulomb coupling between excitons and trions. Remarkable changes to the reflectivity of the polariton device thus occurs as background carrier is modulated.</p> | 51 |

- 4.2 Modifications to exciton-trion-polariton device fabrication. a. Top, MOS-capacitor structure used to control carrier density of MoSe₂ monolayer. Bottom, photonic crystal unit cell. b. FDFD mode simulations of the PC mode with and without hBN. Left, PC mode profile for structure in (a). Mode overlap with Si can be clearly seen. Right, PC mode after added hBN on top of PC. Si loss is reduced, mode profile is higher; resulting in better overlap with monolayer MoSe₂ (not shown). c. Cross-polarized microscope image of fabricated sample. Yellow shade is the Ti/Au contact, while green area is hBN-encapsulated, with the darker green shade in the middle being the device. Circular perturbations to the structure are trapped air bubbles; causing disorder to both photonic and electronic degrees of freedom of the system. 53
- 4.3 Carrier density dependence of exciton-trion-polariton dispersion. a. Dispersion with intrinsically-limited background carrier density. LP-MP bandgap appears almost fully closed. b. Dispersion with $n_e = 1 * 10^{12} \text{ cm}^{-2}$. The LP-MP bandgap opens at 1.618 eV, and $4 \mu\text{m}^{-1}$ c. Dispersion with $n_e = 2 * 10^{12} \text{ cm}^{-2}$. The LP-MP bandgap moves to 1.61 eV, and $3.8 \mu\text{m}^{-1}$ b. Dispersion with $n_e = 4 * 10^{12} \text{ cm}^{-2}$. The LP-MP bandgap further redshifts to 1.59 eV, and to $2.5 \mu\text{m}^{-1}$. This trend is consistent with ETP theory [58] 62
- 5.1 All-optical low-power modulators based on exciton-trion-polaritons. A pump pulse arrives on the sample; photoexcites new carrier pairs, some of which result in a transient net background carrier density. The optical response of polaritons is thus modified when the probe arrives. If the probe pulse is tuned to a part of the polariton dispersion, turning on or off the pump pulse results in modulation of the probe. Efficiency of such a scheme is discussed in the main text. 64
- 5.2 Concept of exciton-trion-polariton metasurfaces. a. Change of real and imaginary optical conductivity with background carrier density. To translate these large optical conductivity changes to large optical response modulation, metasurfaces that optimize mode profile must be engineered. b. A proposed metasurface structure, where the top mirror was "weakened" to pattern the metasurface. How this device could operate as "normally on" or "normally off" all-optical transistors is qualitatively described in the main text. c. Transient metasurfaces by spatial and temporal light modulation. The incoming beam could be shaped to allow a particular pump pulse shape on the sample. This shape will then cause a transient carrier density modulation over the sample, which could then affect optical response of the system to a probe pulse. 67

CHAPTER 1
AN INTRODUCTION TO TRIONS AND THE TRION-PHOTON
INTERACTION PROBLEM

The nature of interactions between light and correlated many-body states in semiconductors has become a point of academic interest contemporary to the development of atomic, molecular, and optical physics as a formal discipline of research. The theory of trions, despite its early introduction to the field of many-body physics over 60 years ago [38], is still actively being investigated. Experimental studies of trions had to wait for a few decades, until the development of high-quality epitaxial films. Once quantum well structures could be realized in III-V materials, experimental signatures of trions were found [30]. However, despite nearly 30 years having passed since trions were experimentally shown, constructing a single microscopic theory that accurately described the seemingly paradoxical traits of trions proved challenging: strongly-correlated [22, 60] but tightly bound [31]; showing experimental optical absorption signatures [31, 2] while theoretically being unable to interact with photons [47]; coupling strongly via Coulomb potential [65] as well as to photons [46, 69]. An overview of the theory of excitons was developed would be necessary in the lead-up to the discussion of trions, and why reconciliation of these various aspects of trions proved difficult.

Suppose a charge-neutral semiconductor is brought under optical excitation. If the photon energy is larger than the optical bandgap of the semiconductor, an equal amount of electrons and holes are generated within the semiconductor. If no interactions between the particles take place, each photoexcited carrier behaves like a free particle. However, Coulomb interactions do take place between

photo-excited electrons and holes [27]. These interactions allow electrons and holes to become strongly correlated; to form quasiparticles. Excitons are the most prominent of these, and are formed when a conduction band electron and a valence band hole forms a bound state, as shown in Fig. 1.1a. When exciton-exciton and exciton-majority carrier interactions can be neglected, this two-body picture is extremely accurate in replicating experimental results [26, 27]. It is when exciton-majority carriers are introduced that the two-body exciton model [27] is no longer sufficient. This is the same regime where trions have been identified.

1.0.1 Theory of Trions as 3-body, Fermionic States

Now suppose the semiconductor has is electron-doped and is brought under optical excitation. In this case, equations of motion for the electronic part of the system is expressed in terms of two-body correlation states [22, 27]. These equations, in turn, are coupled to four-body correlation states [27]. Thus, a recursive relation is established [27, 32]. Typically, the recursive relation is truncated at the two-level equation, while the prominent four-body terms are reduced to product terms of two-body correlations to obtain the Schrödinger Equation for the exciton [27, 32]. Meanwhile, early theories of trions were somewhat ad-hoc; bound three-particle correlations [11, 44, 10, 47], as depicted in Fig 1.1b were introduced and solved for. However, there were numerous issues with this three-particle picture.

First, three-body trion states are fermions. Photons and fermions are both bosons [22], so photo-excitation of excitons conserves boson number. However, in the case of trions, a boson would be generating a fermion; which conserves

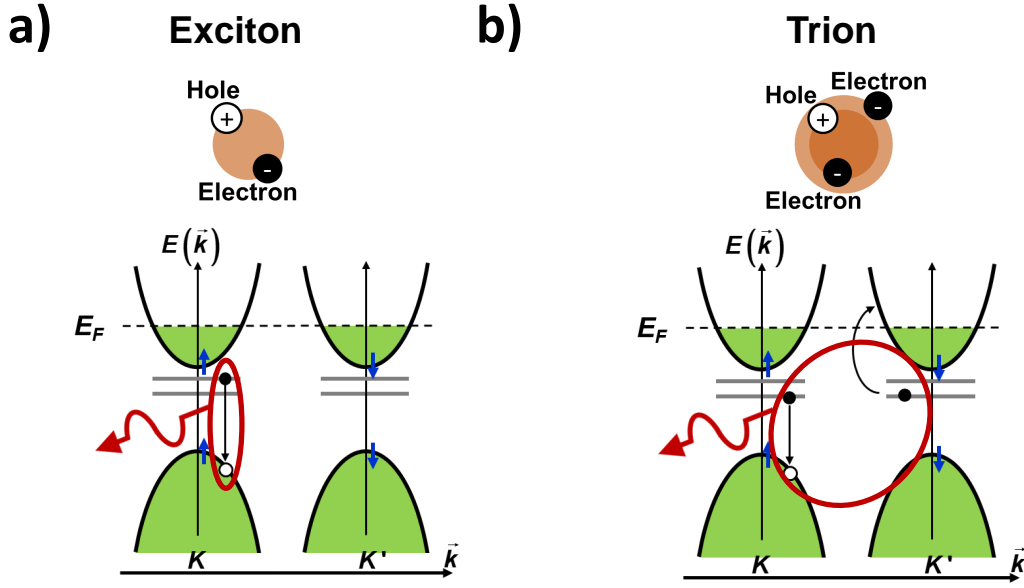


Figure 1.1: Real-space and momentum space representations of excitons and trions in an electron-doped TMD monolayer, according to the three-particle model of trions. a. A bound state formed between a photo-excited conduction band electron, valence band hole pair results in an exciton state. In momentum space, this electron-hole pair, possessing a finite momentum, is shown by the red ellipse. K and K' valleys correspond to the two spin-valley configurations in TMDs. The exciton state can also be formed in the K' valley. Photon emission conserves linear and angular momentum b. The trion state, constructed as a three-particle state comprised of two conduction band electrons, and one valence band hole. The extra electron belongs to the opposite K valley. To conserve total momentum upon photo-emission, the electron in the opposite K' valley has to scatter above the Fermi level.

neither boson nor fermion number [11]. Second, the optical matrix element for a transition from the material ground state to the three-body trion state would be zero [47]. This would result in a trion state that has no spectroscopic signature associated with it, which fails to explain the secondary resonant absorption feature seen in experiments by others [31, 2], as well as discussed in Chapter 2 of this work. Another point discussed in Chapter 2 is the separation between spectroscopic features commonly associated with excitons and trions, which has been shown to depend linearly on the Fermi level of the system [31, 2]. The

three-body state is also impervious to changes in background carrier density, and thus fails to capture the dependence of the exciton and trion resonances on the Fermi level.

Trion-Polaritons

When a photon is trapped in a cavity for long enough to resonantly exchange energy with excitons, the eigenstates of the system are neither excitons nor photons; but mixtures of the two, called exciton-polaritons [75, 52, 41, 28, 18, 5, 69, 66, 9, 33]. The coherent energy transfer between photons and excitons is shown in Fig 1.3a. One final issue about trions emerges in the strong optical coupling regime, where the three-body theory suggests trions should not interact with photons [47, 68], while experiments seemed to suggest otherwise [59, 46, 31]. Furthermore, the three-body trion state does not conserve momentum as it is photo-generated, as shown in Fig. 1.2b. This means that interactions between trions and photons, even if it somehow occurred, were not coherent according to the [68].

1.0.2 Fermi-Polarons Instead of Trions?

Despite all these issues, the three-particle theory of trions persisted until recent years [67]. One reason for this is that models based on three-particle states were able to accurately calculate trion binding energies [44]. Recently, a different approach to the trion problem gained much success [46, 60, 13]. Rejecting the three-particle state picture completely, this method found that for an n-doped (p-doped) semiconductor, interactions between excitons and a two-

dimensional electron gas (hole gas) were found to split the single exciton resonance into two spectral lines. The lower-energy and upper-energy lines, previously attributed to trions and excitons, were associated instead with attractive and repulsive Fermi-polarons [13]. Real-space diagrams for these two polaron states are shown in Trion resonance, meanwhile, was predicted not to have a unique optical signature [46]. By treating the exciton-electron interactions in the many-body regime, this theory was able to explain the dependence of exciton and "trion" resonances on the Fermi level [46]. One serious drawback of the Fermi-polaron polariton theory is that it introduces artificial maximum energy and momentum cutoff frequencies in computations of optical conductivity; restricting the accuracy in determining the absolute trion binding energies [13].

a) Attractive Polaron b) Repulsive Polaron

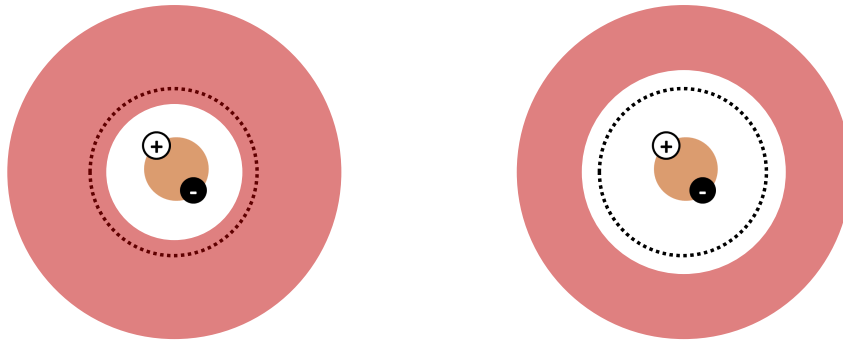


Figure 1.2: Real-space representations of attractive and repulsive Fermi-polaron states. a. Attractive Fermi-polaron. The electron cloud (shown in red) surrounding the exciton is brought closer to the exciton due to Coulomb interactions. b. Repulsive Fermi-polaron. The electron cloud (shown in red) surrounding the exciton is pushed away further from the exciton due to Coulomb interactions.

1.1 A Novel Theory of Trions as 4-Body, Bosonic States

At low carrier densities, the Fermi-polaron model has been approximated by the two-body exciton model, which precludes contributions of trions to the optical conductivity [13]. However, recent work by Rana et al [22] has shown that not to be complete. In this work, excitons were described two-particle bound states formed by a conduction band electron and a valence band hole; similar to other works [47]. However, a four-body bound state, which is formed by a conduction band electron-conduction band hole pair in addition to the conduction band electron-valence band hole pair was also postulated to exist [22]. In order for exchange interactions to be favorable to this bound state forming, the interband and intraband electron-hole pairs must belong to opposite K valleys, as shown in Fig 1.3b [22].

These two states emerge directly from solving the 2DEG Hamiltonian with electronic and optical interaction terms. The solution is comprised of two separate Schrödinger Equations. The first equation is for a two-particle correlation state, while the second is for a four-particle correlation state [22]. The eigenstates of these two equations correspond to the exciton and trion states, respectively. Crucially, Rana et al. concludes that the two Schrödinger Equations are coupled [22]. The strength of coupling is proportional to the Fermi level, so if the 2D semiconductor is electron- or hole-doped, the eigenstates of the system are not excitons and trions, but instead exciton-trion superposition states. Furthermore, the splitting energy of these exciton-trion superposition states depends on the Coulomb coupling strength, correspondingly, on the Fermi level. This linear dependence is consistent between various many-body theories of exciton-electron interactions [60, 13, 22] and has been verified experimentally

[31, 2].

Four-particle trions as constructed by Rana et al. correctly reconcile various aspects of the three-particle, and Fermi-polaron theories. First point stems from the real-space configuration of four-particle trions, which is shown in Fig 1.3b. Here, the interband electron-hole pair, and the electron of the intraband electron-hole pair is situated close to the center of mass while the conduction band hole ends up much further from the center of mass. The radius of the conduction band hole, also referred to as the exchange-correlation hole, is inversely proportional to the Fermi momentum [22]. Thus, when the background carrier density is negligible, the exchange correlation hole radius is very large; resulting in a state whose dynamics could be approximated by the three-particle trion model. Secondly, four-particle trions, though they are bosons, have a zero matrix element with the material ground state [22]. So, any photon-trion interactions have to be mediated by the presence of excitons. So, even though the four-particle trion state is an eigenstate of the Hamiltonian at any carrier density, the oscillator strength associated with the lower exciton-trion resonance is zero when background carriers are not present [22]. The oscillator strength transfers from the upper exciton-trion resonance to the lower one as Fermi level is increased [22], consistent with experimental observations that will be discussed in Chapter 2 and were reported elsewhere [2].

It is important to note that not all four-particle correlation states correspond to bound trions. Instead, at large carrier densities, exciton-electron scattering states, also referred to as unbound trions, become more favorable to Coulomb interactions with the exciton than does the bound trion states. Thus, at the large carrier density limit, solutions of the coupled Schrödinger Equations is consis-

tent with the Fermi-polaron picture [22].

1.1.1 Exciton-Trion-Polaritons

The complete diagram of interactions between photons, excitons, and bound and unbound trions looks like Fig 1.4a. For a doped 2D semiconductor in the strong optical coupling regime, neither the optical coupling between photons and excitons, nor Coulomb coupling between excitons and trions could be ignored. In this regime, eigenstates of the system are coherent superpositions of photon, exciton, and trion states [58]. Fascinatingly, these states, called exciton-trion-polaritons, are expected to coherently exchange energy between photon, exciton, and trions [58]. This is a crucial point, as trion-polaritons according to the three-particle picture cannot coherently exchange energy. How the coherence is lost is shown in Fig. 1.4b, while Fig 1.4c shows how energy is coherently exchanged between trion and photons (via excitons).

The point of coherence is also a very important one from an experimental point of view, since recent works has brought to attention [23] coherent quantum beats between exciton and trion resonances, which would be expected by the exciton-trion-polariton formalism at the weak optical coupling limit [58].

In analogy to the coupled-oscillator model commonly employed in the analysis of exciton-polaritons [37], the eigenstates of the coupled exciton-trion-polariton system can be modeled as an infinite matrix, shown in Eq 1.1:

$$\left(\begin{array}{cccccc}
\hbar\omega(\vec{Q}) - i\gamma_{ph} & \frac{1}{2}\hbar\Omega^{ex} & 0 & 0 & 0 & 0 & \dots \\
\frac{1}{2}\hbar\Omega^{ex} & E^{ex}(\vec{Q}) - i\gamma_{ex} & M_b & M_{1,ub} & M_{2,ub} & M_{3,ub} & \dots \\
0 & M_b & E_b^{tr}(\vec{Q}) - i\gamma_{tr} & 0 & 0 & 0 & \dots \\
0 & M_{1,ub} & 0 & E_{1,ub}^{tr}(\vec{Q}) - i\gamma_{tr} & 0 & 0 & \dots \\
0 & M_{2,ub} & 0 & 0 & E_{2,ub}^{tr}(\vec{Q}) - i\gamma_{tr} & 0 & \dots \\
0 & M_{3,ub} & 0 & 0 & 0 & E_{3,ub}^{tr}(\vec{Q}) - i\gamma_{tr} & \dots \\
\vdots & \vdots & \vdots & \vdots & \vdots & \vdots & \ddots
\end{array} \right) \quad (1.1)$$

where the first three diagonals show the coupling between photon, exciton, and bound trion states, respectively. Remaining of terms are unbound exciton states, which form a continuum. Each unbound trion state's Coulomb coupling to the rest of the system is an independent coefficient that was computed by Rana et al. [22, 58]. The matrix element for bound trion-photon coupling, as previously mentioned, is zero. This model is illustrative, since some theoretical treatments of charged-exciton-polaritons incorrectly include photon-trion mixing terms into their model (a common name for exciton-trion-polaritons) [12].

For a quantitative determination of exciton-trion-photon dispersion, calculating the photon Green's function [58] is very helpful:

$$\begin{aligned}
G^{ph}(\vec{Q}, \omega) &= \frac{1}{\hbar\omega - \hbar\omega_{PC}(\vec{Q}) + i\gamma_{PC} - \Sigma^{ph}(\vec{Q}, \omega)} \\
\Sigma^{ph}(\vec{Q}, \omega) &= -i\hbar \frac{|\xi(z_{ML})|^2}{2 < \epsilon >} \sigma_{2D}(\vec{Q}, \omega)
\end{aligned} \quad (1.2)$$

Here, $\Sigma^{ph}(\vec{Q}, \omega)$, the photon self energy term, determines the optical interaction strength and is proportional to optical conductivity σ_{2D} , as well as the

mode overlap factor $\xi(z_{ML})^2$ [58]. Qualitative features of polariton dispersion measurements, resonance energies and linewidth, could then be related to the theory using the model below:

$$R(\vec{Q}, \omega) = |1 + B * G(\vec{Q}, \omega)|^2 \quad (1.3)$$

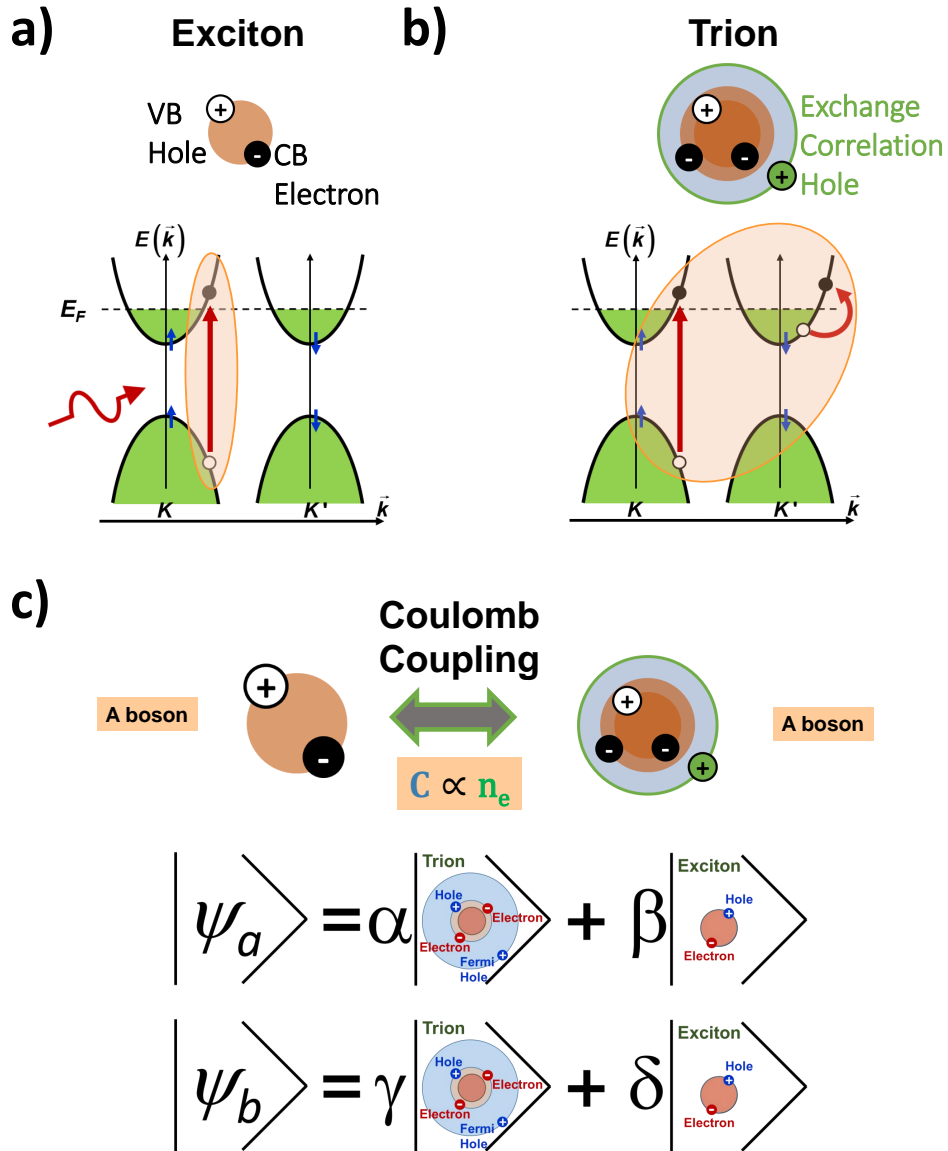


Figure 1.3: Two- and four-particle bound states and their interactions according to [22]. a. Exciton state. The interband electron-hole pair is shaded in orange. b. Bound trion state. An interband electron-hole pair combined with an intraband electron-hole pair that forms the state is shaded in orange. Here, the hole shown in green is the conduction band hole, which is also referred to as the exchange correlation hole. For the bound trion state to be correctly analyzed, Coulomb interactions between the exchange correlation hole and the other three particles need to be considered. c. Exciton-trion superposition states due to Coulomb coupling. Strength of the Coulomb coupling depends on n_e , the background carrier density. Eigenstates of the system, denoted as a and b here, are coherent exciton-trion superposition states.

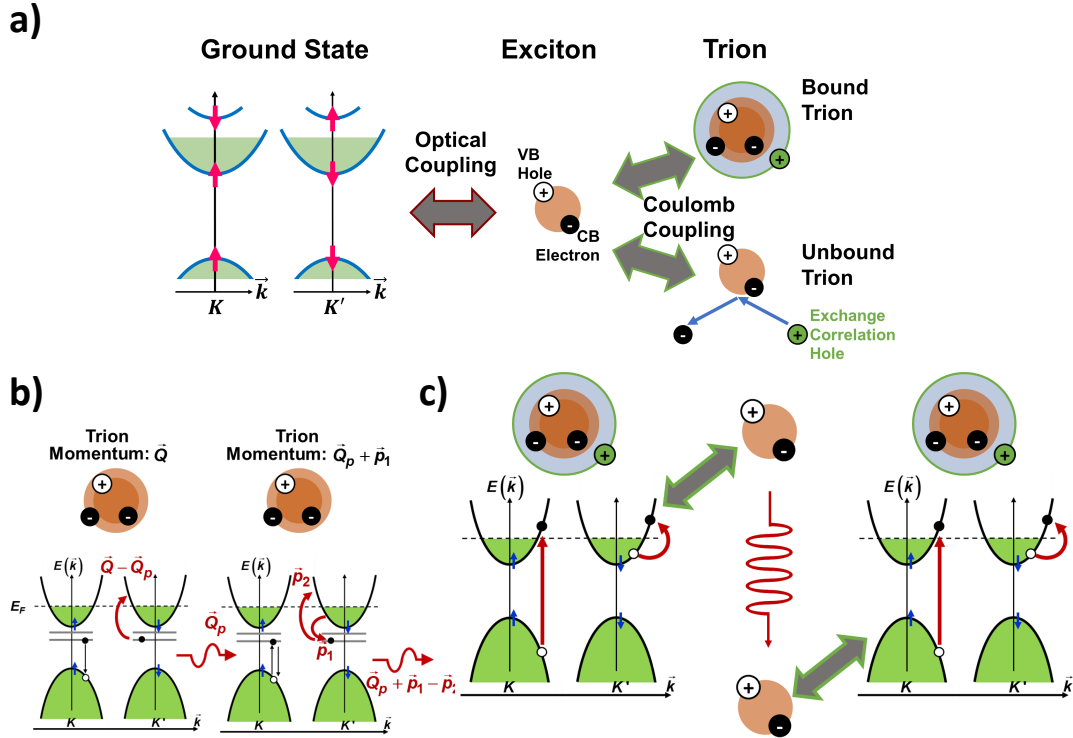


Figure 1.4: Exciton-trion-polaritons in 2D semiconductors. a. A complete model of coupled oscillator interactions that describe exciton-trion-polaritons. The optical coupling between ground state and exciton is then followed by Coulomb coupling between excitons, and bound or unbound trions. A coherent superposition state can form between excitons, bound trions, and photons. Unbound trion states form a continuum, which is one of the mechanisms that reduces the lifetime of these coherent states [57]. b. A description of why the three-particle trion model does not predict coherent trion-polaritons. When a trion of certain momentum emits a photon, the second CB electron ends up above the Fermi level. Meanwhile, the new CB electron taken from the Fermi sea lies beneath the Fermi level; necessitating a change in trion momentum after the photon is reabsorbed. Coherence of trion-photon interactions are quickly lost. c. How a coherent exciton-trion-polariton state is formed. Due to Coulomb interactions, the trion couples to an exciton state. This exciton state emits, and reabsorbs a photon, and then couples back to the first trion state. Thus, the trion-photon interaction, while indirect, is entirely coherent.

CHAPTER 2

OPTICAL CONDUCTIVITY OF MONOLAYER MOLYBDENUM DISELENIDE

Subtle differences between theories discussed in Chapter 1 requires precise spectroscopy experiments and a quantitative analysis of the results. Such an analysis cannot begin unless optical conductivity is determined. As discussed in Chapter 1, when the optical conductivity is determined, it allows accurate simulation and modeling hybrid photonic-matter systems; even in the strong-coupling limit.

Another critical choice that has to be made before the start of experimental investigation is the choice of the material system. In what choosing materials are best-suited for spectroscopy of exciton-trion superposition states, the largest trion binding energy (the splitting energy between the two exciton-trion superposition states) is one of the most important factors: besides allowing for accurate spectroscopy, the large trion binding energy prevents dissociation at increased temperatures; increasing the thermal budget of spectroscopy measurements due to optical absorption and subsequent heating. Exciton and trion binding energies are generally proportional, so the exciton binding energy is the common figure of merit that guides the material of choice for trion spectroscopy: this energy could be as large as ~ 30 meV in III-V quantum wells in the 2D limit [26], and in III-Nitride materials [51], while it is over 300 meV in TMDs [31]. This remarkable increase in exciton binding energy is consistent across various TMDs, and is related to the reduced 2D electron screening in TMDs compared to the 3D electron screening of quasi-2D GaAs quantum dots [27].

Monolayer Molybdenum Diselenide (MoSe_2) was the TMD chosen for the

investigations discussed in Chapters 2-4. While the exciton absorption of the material is not as large as that of other TMDs [78], its photoluminescence spectrum being predominantly due to bright excitons [45], a trion binding energy of ~ 30 meV [20], a typical emission linewidths of ≤ 10 meV [48, 50, 29], a relatively large conduction band spin-valley splitting [20] combine to make it extremely attractive for spectroscopic studies of trions.

2.1 Measurement of Optical Conductivity of Monolayer MoSe₂

Optical conductivity is measured with the help of a steady-state reflection spectrum. These measurements are some of the most basic of among optical spectroscopy measurements. However, proper care needs to be taken to ensure results obtained from these measurements are accurate, and thus can be used to confirm novel condensed matter theory. Figure 2.1a shows a cartoon diagram of the device, and how the measurement is normalized. A top-down image of the device is shown on Fig 2.1b. Before a detailed description of experimental techniques, it is important to discuss how high-quality MoSe₂ devices are fabricated.

2.1.1 Fabrication and Deterministic Dry-Transfer of 2D-Layered Materials

Fabrication can be broadly separated into three parts; exfoliation and identification of monolayer MoSe₂ and 50 – 150 nm thick hBN flakes, deterministic dry transfer of the monolayer flake onto a high-quality dielectric film, and

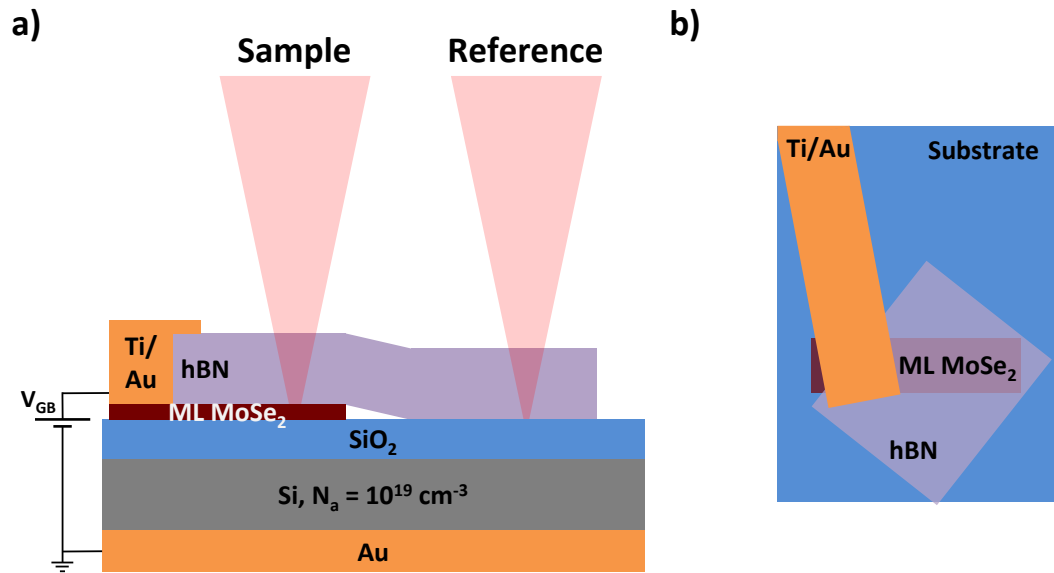


Figure 2.1: Encapsulated monolayer MoSe₂ capacitor device used in carrier-density-dependent optical conductivity measurements. a. Side-view of the device, along with the measurement scheme. The monolayer is directly exfoliated on the SiO₂ layer, and is encapsulated by hBN. Ti/Au contacts are deposited on the exposed portion of the monolayer. Normalized reflectivity measurements are done by a confocal reflectance measurement on the sample, and normalized by a confocal reflectance measurement on the hBN encapsulated oxide substrate. The ratio of these measurements is then compared to the calculated transmission spectrum. b. Top-down view of the sample.

fabrication of titanium-gold (Ti: Au) contacts to the monolayer. For these measurements, high-quality Si/SiO₂ substrates were purchased from a commercial vendor. Si substrate was p-doped with B atoms with a hole density of $10^{19} - 10^{20} \text{ cm}^{-3}$. These high doping densities are chosen with the intent of preventing carrier freeze-out at low temperatures. Meanwhile, the oxide thickness of 90 nm was chosen in order to enhance reflection contrast due to the excitonic resonances of the monolayer MoSe₂ [74].

Exfoliation and Identification of MoSe₂ Monolayers and hBN

There are probably as many techniques for exfoliation of monolayers as there are different researchers working on 2D materials. Due to the non-repeatable and statistical nature of exfoliation, variations in bulk crystals, exposure over time to ambient oxygen and humidity, and other factors make exfoliation difficult to discuss in precise terms. However, it is still possible to go over the author's best accumulated practices in the lead-up up to this thesis. As TMDs are much more brittle than graphene, Nitto Denko tape was chosen over standard Scotch tape typically employed for exfoliation. Fig 2.2a shows how the tape is shaped into a long strip with non-adhesive ends for handling. Fig 2.2b shows commercially-purchased bulk MoSe₂ flakes, which were grown by the vendor using a flux-zone method to contain minimal defects or extrinsic dopants [14]. A small portion of the monolayer is cut, and populated onto the entire Nitto Denko tape as shown in Fig 2.2c. Since MoSe₂ flakes degrade in ambient air [63], multiple dry-transfer stamps were made (Fig 2.2d) and MoSe₂ exfoliated onto the stamps (Fig 2.2e).

Dry-transfer stamps were made by cutting 2 cm-wide square gel-pak adhesive tape sections, peeling the tape portion out from the non-adhesive covers of the gel-pak tape (inset, Fig 2.2d), and placing the tape onto high-quality microscope slides. It is important that the tape sits on the slide without any air bubbles present, since air bubbles will result in a potential failure of the subsequent dry-transfer step. While it has been recommended [1] that a slight UV/Ozone treatment of the dry-transfer stamp should improve monolayer quality due to reduction of contaminants, no significant advantage has been seen in this work.

The only remaining step is to find monolayer flakes and label them. Vari-

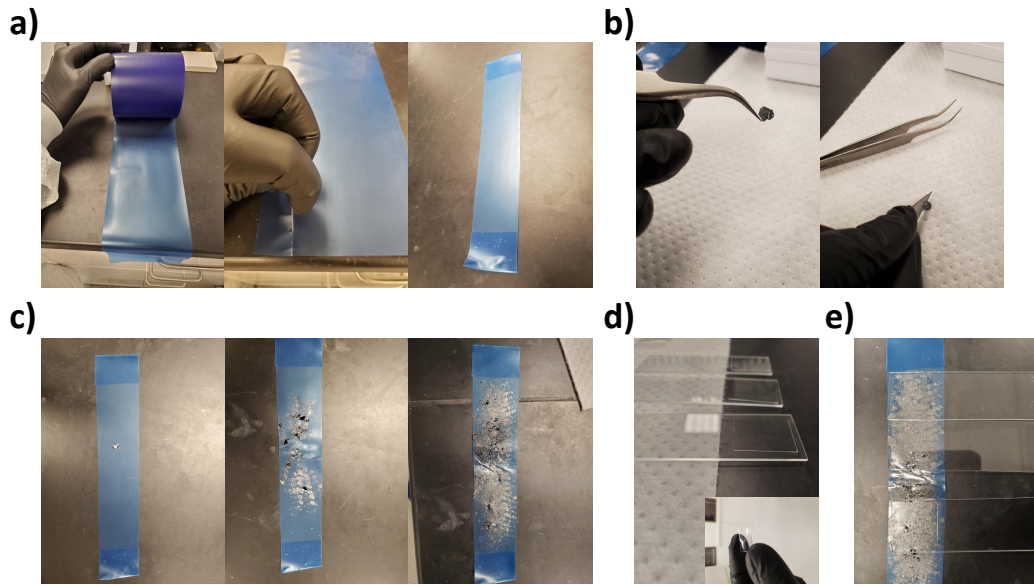


Figure 2.2: Summary of dry transfer step preparation. a. Nitto-Denko tape is cut into strips, and edges are folded. b. A small section is cut from a large, shiny, and recently-opened flake of bulk, flux-zone-grown MoSe₂. c. The tape is populated until a smooth, shiny film covers the whole tape. d. PDMS stamps are placed on high quality microscope slides. Slides are rinsed to remove dust specks that can come between PDMS and glass. PDMS films should be bubble and wrinkle-free for best device yield. e. PDMS stamps are flipped and placed over the populated blue tape. Mild pressure is applied to push air out of contact area. After one minute, stamps are carefully peeled from tape.

ous methods of distinguishing monolayer flakes from those of multilayer ones have been developed. Besides atomic-force microscopy, Raman spectroscopy signatures unique to monolayers [6] could be used to identify monolayers of TMDs. Meanwhile, a ~ 40 times increase in photoluminescence efficiency is one of the most reliable methods of finding monolayers of MoSe₂ [7]. Once reliable practice is obtained, it is fairly straightforward to distinguish monolayer flakes solely by optical contrast. A device candidate flake's PL is always tested at low temperature, so only monolayers make it to becoming a device.

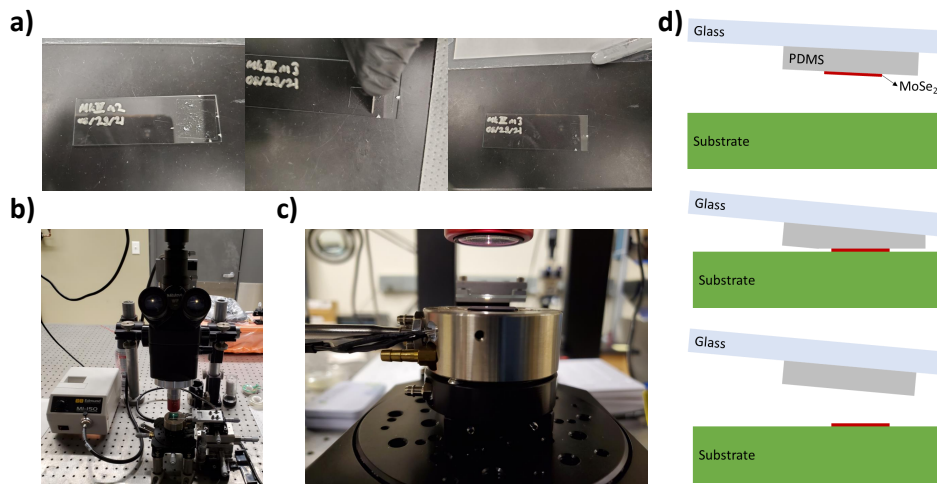


Figure 2.3: 2D transfer process and setup. a. Desired flakes on the device are approximately marked in two orthogonal axes using a silver marker. A 1 mm² area around the flake is then cut. b. A photograph of the 2D transfer setup. While oxygen damage is well-studied in literature, this transfer setup did not employ a glove-box as devices were fabricated within 24 hours of the flakes being exfoliated. c. Close-up image of the microscope, the transfer slide, sample, and hot plate the sample is placed on. d. A depiction of how the PDMS film transfers the flake on the substrate. The three stages of how the PDMS is shaped is approximate, but the curvature of PDMS could be easily determined by interference and color contrast on the microscope image. All dry-transfer processes took place at 46 °C.

Dry Transfer of 2D Materials onto Substrate

Once MoSe₂ and hBN Flakes of desired quality and size are found, they need to be assembled over the substrate. Assembly begins by taking two high-resolution microscope images of each flake. The high-magnification image helps as a means checking if subsequent fabrication damaged the 2D material; the low-magnification image, combined with marks on the glass slide made with a silver marker pen help to easily find the desired monolayer. Once the flakes are identified, the PDMS square stamps are cut down with the flake in center. If the cutting process is done improperly, the PDMS stamp holding the flakes can suffer large strain, thus damaging the flake itself. Key steps in this process are

shown in Fig 2.3a. Reducing the stamp size, despite the aforementioned risk, is crucial for the subsequent dry transfer step, which was accomplished with a custom modified microscope shown in Fig 2.3b. Here, the substrate is placed on the temperature-controlled stage, shown up close in Fig 2.3c. Once the substrate is heated to 45 °C, the glass slide holding the 2D material flake is placed facing down. As shown in Fig 2.3d, a slight contact angle of $\sim 1^\circ$ is maintained between the slide and the substrate. The slide is then lowered until the contact front goes past the flake area. After a minute of waiting, the slide is retracted gently, leaving behind the flake on the substrate. Fully encapsulated devices can be realized by repeating the above process successively for hBN, monolayer MoSe₂, and hBN flakes. There are some drawbacks with this technique; namely, failure of the flakes to stick to the substrate, and contamination introduced between each flake facet due to the PDMS-facing sides of each flake. Alternative techniques [21] that have led to tremendous improvements in device quality, but were not used towards this thesis, are discussed in the Appendix.

Photolithography of Contacts

After dry transfer steps are complete, part of the monolayer is purposefully left exposed similar to the top-down view shown in Fig 2.1b. This exposed opening is where planar Ti:Au contacts are defined on top of the exposed monolayer area, and deposited using a single-step photolithography process, details of which are given in Table 2.1. After photolithography is complete, the devices are glued onto a ceramic chip to which Ti:Au contacts are wire-bonded.

While the fabrication is quite straightforward, there are a few points about device quality worth discussing. First, the exposed monolayer runs the risk of

Table 2.1: Photolithography of Metal Contacts

| Step | Description | Details |
|------|-------------|--|
| 1 | Spin | AZ nLOF 2020, 4000 RPM, 1000 RPM/s acceleration, 60s |
| 2 | Softbake | 110 °C on Hot Plate, 60s |
| 3 | Expose | 5s on ABM Contact Aligner (g-line of lamp) |
| 4 | Hardbake | 110 °C on Hot Plate, 60s |
| 5 | Develop | AZ 726 MIF, 60s, immerse in DI water, blow-dry |
| 6 | Evaporate | 20 nm Ti, 160 nm Au |

allowing water and other solvents to intercalate between hBN and the MoSe₂ flake [53]. Microscope images of the devices that were used in this measurement were taken before and after lithography with the expectation that even a few-nm liquid solvent intercalating between hBN and monolayer MoSe₂ other disorder introduced during fabrication would cause a large optical contrast change in the post-fabrication images at the locations of disorder. However, no change has been observed in microscope images post-fabrication. As an added benefit, hBN encapsulation possibly reduces ambient air adsorption by the monolayer, which prevents long-term device degradation [63, 20]. The second point concerns the quality of contacts. It has been pointed out that due to the work function mismatch of MoSe₂ to Ti and other contact metals [77], metal-TMD junctions tend to show rectifying behavior instead of Ohmic [77]. One notable exception where reliable Ohmic contacts has been obtained is 1D edge contacts [73]. Also, a choice has been made to not anneal the devices after contact deposition. One reason for this decision is due to reports where metal-TMD junctions were not improved by annealing [76], and also due to concerns among the polariton community against detrimental effects of annealing on the TMD monolayer [46]. This admonition is well-warranted, as experimental evidence of exciton localization around intrinsic defects after annealing abound [24, 63]. How the metal-TMD junction affected exciton-trion, and exciton-trion-polariton

systems was left for future investigations.

For the devices discussed in this work, measurements were done in steady-state and included large induced carrier densities. Furthermore, as will be discussed later in this Chapter, accurate fitting of the results allowed the carrier density to be extracted, and then compared to the carrier density expected from a perfect MOS capacitor in equilibrium. Thus, results in this section were analyzed as if no imperfect lateral junctions existed in the device. Despite all this, a systematic study of contact quality on exciton-trion-polariton devices should be an immediate priority of future research for similar systems.

2.1.2 Experimental Setup

Measurements of carrier-density-dependent MoSe₂ optical conductivity were realized using a home-built low-temperature confocal microscopy setup. Characterization of samples was through PL, which was excited with a continuous-wave, 532 nm pump laser. PL is greatly enhanced going from multilayer monolayer MoSe₂ [7]. Furthermore, the lineshape of the two PL emission lines is related to the exciton and trion lifetimes, in the manner described by many-body trion model [57]. These PL measurements are qualitative; that is to say, absolute quantum efficiency is not characterized. So, the pump laser beam was not made confocal with the rest of the setup. However, optical conductivity measurements are not done through PL but reflection; which requires precise alignment of the setup.

Reflection spectroscopy can be performed with quantitative accuracy, and as will be discussed in the next section, modeled rather accurately with a fairly

simple model. To realize quantitative accuracy of reflection measurements, the experimental setup was built to best accommodate the following:

1. Precise alignment of the confocal microscope setup that the white light source is then aligned to.
2. Minimizing mechanical noise and setup drift.
3. Ensuring minimal thermal and mechanical noise due to cryogen transfer.

A diagram of the setup is shown in Fig 2.4a. Confocal microscopy requires a good deal of care to ensure repeatable, quantitatively accurate results. In the Rana group setup, a PL pump laser was used to define the optical axis of the microscope. Once this alignment was satisfactory, the sample was placed in the microscope focus. Due to slight chromatic aberrations of practical optics, the optimal focus depended on the wavelength. Formation of a clear image on the camera placed immediately after the objective (not shown) was assumed to be the ideal focus position. The laser light reflected from the substrate allowed alignment of spatial filter, and monochromator optics. Due to the focusing and collimating optics used in the spatial filter, sample tip and tilt has detrimental effects on the image quality after the spatial filter. Sample tip and tilt can be minimized by removing the objective, and confirming that the laser reflected from the sample travels along the same path as the optical axis of the setup. To spatially filter stray/defocused/scattered light, a pair of lenses were brought to the same focus, and a pinhole was placed at the focal plane of the lenses. Alignment of the monochromator and CCD is discussed in the Appendix. Once alignment was perfected, the device, having already been placed under high vacuum, was connected to the biasing circuit, and cooled down via liquid helium.

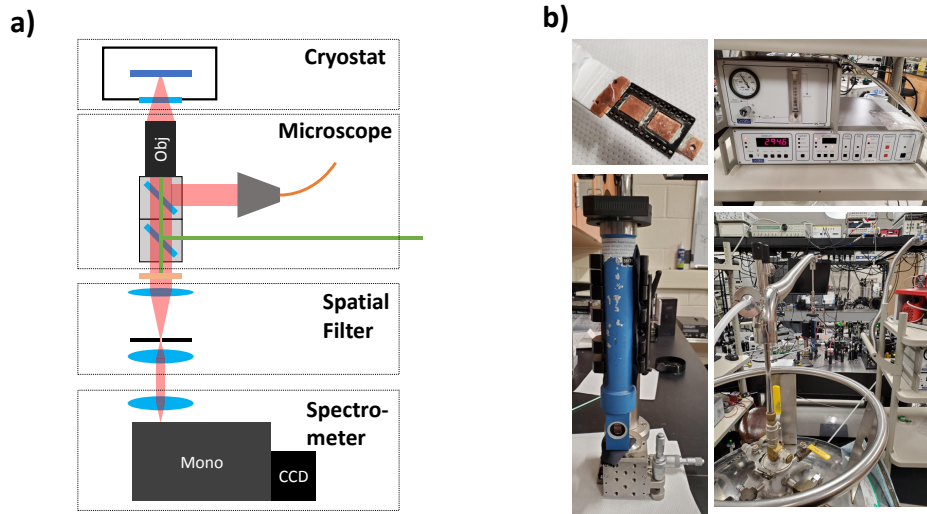


Figure 2.4: Diagram and photographs of the optical spectroscopy measurement setup. a. The microscope section depicts the white light, shown in red, being collimated out of the multimode fiber and refocused onto the cryostat. The reflected light passes through the spatial filter, which accepts only collimated light, and enters the spectrometer. b. Photos of the setup. Clockwise from top left: The cryostat cold finger chip socket. Packaged devices mate into this socket, and can thus be electrically controlled via a bias circuit (not shown) outside the cryostat; He flow and temperature control electronics for the cryostat; the setup at work; the x-y-z stage mount for the cryostat. The cryostat is held by numerous clamps, which minimizes vibrations. To further minimize vibrations, the pressure points between clamps and the cryostat are separated by a soft tissue, which reduces pressure and increases force on the cryostat. The clamps are held by a vibration-dampening post. Furthermore, the cryostat is supported from below by a metal post with another tissue between the cryostat and the metal post. Care was taken to ensure the center of gravity lies within the transfer stage. The post was placed towards the fixed point of the 2D transfer stage to ensure minimal vibrations.

Fig 2.4b shows the cryostat on the top left, the home-built biasing circuit integrated onto the cryostat tail on the bottom left, the Oxford low-temperature control circuit on the top right. Under operation, the complete system appears as shown on the bottom right of Fig 2.4b. The aforementioned three design criterion for the setup become important for optical conductivity measurements for various reasons. Sample non-uniformity commonly seen in TMD devices [15] result in a need for either spatially-resolved measurements, or for all carrier-

density-dependent measurements to take place in roughly the same area. Due to the poor lateral contacts between Ti/Au and monolayer MoSe₂, minutes-long transients elapse before the device reaches steady state at a new gate voltage, requiring about 15 minute intervals for each of 35 carrier density measurements. The procedure used to ensure minimal drift and mechanical noise in low-temperature measurements is described in further detail in the Appendix.

2.2 Measurement, Results, and Analysis

The measured, normalized reflection spectra is shown on Fig 2.5a as a function of gate voltage. A brief glance at the measurement shows two resonances appearing as dips in normalized reflectivity. Each resonance has 5-10 meV linewidth, consistent with PL measurements. Increasing negative gate voltage bias results in larger background electron density and an increased Fermi level. With a more careful look, it is possible to see that the splitting energy of the two resonance peaks increase with Fermi level. This effect cannot be explained by the three-body trion picture; rather, it requires a many-body treatment. Exciton-trion superpositions states introduced in the introduction are able to precisely explain the trend of peaks shifting with increasing voltage. While qualitative agreement between experimental results and many-body trion theory is very exciting, a quantitative treatment is needed to better explain how closely theory and experiments agree. The rest of this section discusses quantitative analysis of the results.

In the most general case, optical conductivity cannot be uniquely determined by only reflection spectra, except when the Kramers-Kronig (KK) trans-

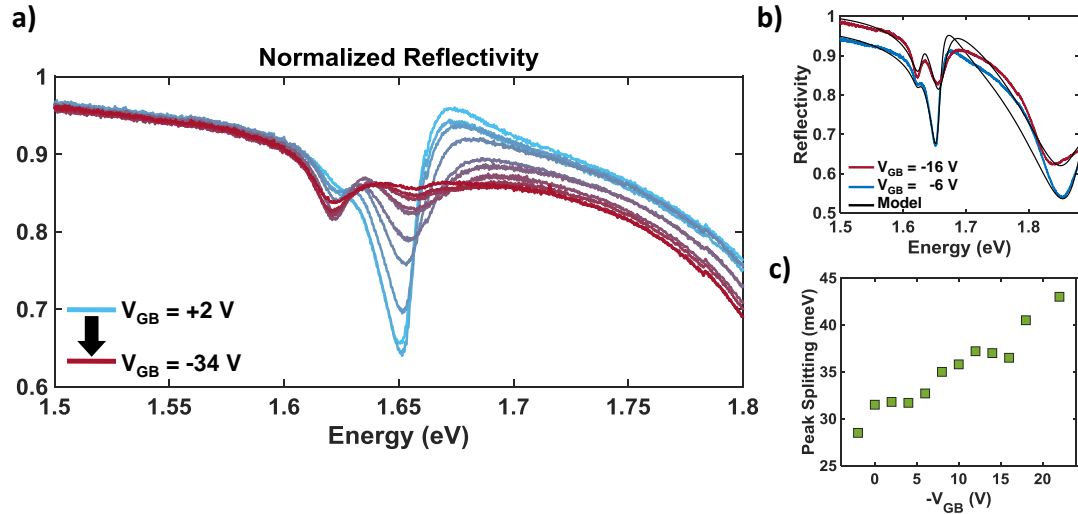


Figure 2.5: Normalized reflectivity, optical conductivity fits, and linear dependence of Fermi level and carrier density. a. Evolution of the normalized reflectivity as bias voltage is decreased from +2V to -34V (carrier density changed from intrinsic levels to large n-doping). The large resonance at 1.65 eV disappears as carrier density is increased. Conversely, a second resonance, unseen at intrinsic carrier densities, emerges as carrier density increases; eventually becoming larger than the resonance at 1.65 eV. b. Fits of two select carrier densities using the transfer-matrix model based on optical conductivity spectra of [22]. In order to approximately fit the feature at 1.8 eV, possibly due to B-exciton absorption, two phenomenological resonances were introduced to mimic B-exciton, and bandgap absorption. These did not affect the reflectivity contrast at 1.65 eV or below greatly; so did not change the physics being discussed. c. Using best fits, examples of which were shown in (b), dependence of splitting energy between upper and lower exciton-trion resonances, and gate voltage was measured. The device is in accumulation mode, so gate voltage and carrier density are linearly proportional. Since carrier density and Fermi level are proportional, the measured peak splitting is approximately linear with Fermi level, as predicted by various theoretical works. [60, 13, 22].

form is used to relate real and imaginary optical conductivity spectra [78]. For the measurements, experimentally obtained reflectivity can be compared against a computed spectrum where the optical conductivity of the monolayer is derived by theory. To obtain the computed reflectivity spectrum, a simple thin-film transmission matrix model can be employed. For a thin film of thickness L_2 that is has a medium of index n_1 to its left, and n_2 to its right, Eq. 2.1 is

the transmission matrix.

$$\begin{pmatrix} \frac{n_1+n_2}{2n_1} & \frac{n_1-n_2}{2n_1} \\ \frac{n_1-n_2}{2n_1} & \frac{n_1+n_2}{2n_1} \end{pmatrix} * \begin{pmatrix} e^{(-2\pi L_2 * n_2 / \lambda)} & 0 \\ 0 & e^{(2\pi L_2 * n_2 / \lambda)} \end{pmatrix} * \begin{pmatrix} \frac{n_2+n_3}{2n_2} & \frac{n_2-n_3}{2n_2} \\ \frac{n_2-n_3}{2n_2} & \frac{n_2+n_3}{2n_2} \end{pmatrix} \quad (2.1)$$

Using commercial, microscope-based reflection measurement setups, and a fitting procedure based on the matrix model described above, thicknesses of SiO₂ and hBN layers can be verified. Refractive index of SiO₂ was confirmed to be close to 1.42, the value for a stoichiometric oxide film [61], via spectroscopic ellipsometry. In case of hBN, the refractive index values were taken from [39, 54]. It should be noted that hBN is birefringent; and has noticeable index contrast between in-plane and out of plane orientations [54]. In our model, this was ignored, as only plane waves normally incident on the substrate was considered. Once these index and thickness values were known, the following transmission matrix model was used for the reflectivity of the encapsulated monolayer (see "Sample" section of Figure 2.1):

$$\begin{pmatrix} T_{11}(\lambda) & T_{12}(\lambda) \\ T_{21}(\lambda) & T_{22}(\lambda) \end{pmatrix} = \begin{pmatrix} \frac{1+n_{hBN}}{2} & \frac{1-n_{hBN}}{2} \\ \frac{1-n_{hBN}}{2} & \frac{1+n_{hBN}}{2} \end{pmatrix} \begin{pmatrix} e^{(-2\pi L_{hBN} n_{hBN} / \lambda)} & 0 \\ 0 & e^{(2\pi L_{hBN} n_{hBN} / \lambda)} \end{pmatrix} \begin{pmatrix} \frac{n_{hBN}+n_{ML}}{2n_{hBN}} & \frac{n_{hBN}-n_{ML}}{2n_{hBN}} \\ \frac{n_{hBN}-n_{ML}}{2n_{hBN}} & \frac{n_{hBN}+n_{ML}}{2n_{hBN}} \end{pmatrix} \\ \begin{pmatrix} e^{(-2\pi L_{ML} n_{ML} / \lambda)} & 0 \\ 0 & e^{(2\pi L_{ML} n_{ML} / \lambda)} \end{pmatrix} \begin{pmatrix} \frac{n_{ML}+n_{SiO_2}}{2n_{ML}} & \frac{n_{ML}-n_{SiO_2}}{2n_{ML}} \\ \frac{n_{ML}-n_{SiO_2}}{2n_{ML}} & \frac{n_{ML}+n_{SiO_2}}{2n_{ML}} \end{pmatrix} \begin{pmatrix} e^{(-2\pi L_{SiO_2} n_{SiO_2} / \lambda)} & 0 \\ 0 & e^{(2\pi L_{SiO_2} n_{SiO_2} / \lambda)} \end{pmatrix} * \\ \begin{pmatrix} \frac{n_{SiO_2}+n_{Si}}{2n_{SiO_2}} & \frac{n_{SiO_2}-n_{Si}}{2n_{SiO_2}} \\ \frac{n_{SiO_2}-n_{Si}}{2n_{SiO_2}} & \frac{n_{SiO_2}+n_{Si}}{2n_{SiO_2}} \end{pmatrix} \quad (2.2)$$

A similar T-matrix expression can be used for the "Reference" measurement by simply removing terms pertaining to the monolayer. Once these two transmission matrix expressions are found, the measured normalized reflectivity spectrum is simply:

$$R_{meas} = \frac{R_{Sample}}{R_{Reference}} = \left| \frac{T_{21_{sample}}}{T_{11_{sample}}} \right|^2 / \left| \frac{T_{21_{reference}}}{T_{11_{reference}}} \right|^2 \quad (2.3)$$

L and n are thickness and refractive index values, respectively. Wavelength dependence of refractive index was included in computations, but its effect is negligible. The monolayer MoSe₂ is treated as a thin film, with 0.7 nm thickness [20]. 2D optical conductivity was converted to dielectric permittivity using the following expression:

$$\epsilon(\omega) = \epsilon_{DC} + \frac{i \sigma_{2D}(\omega)}{\omega L_{ML}} \quad (2.4)$$

σ_{2D} is the optical conductivity extracted directly from the many-body trion theory [22], which can be found only by adjusting the optical bandgap and trion binding energies of MoSe₂. To obtain better fits, a low-frequency dielectric constant is added to the monolayer refractive index. Furthermore, to account for the large changes to reflectivity at high frequencies due to B-exciton and inter-band carrier absorption resonances, two phenomenological Lorentzian terms have been added to the 2D optical conductivity. With the introduction of these fitting parameters, which are not strongly changed but only used to increase fit accuracy, the calculated optical conductivity agrees remarkably well with the measured values. This strong agreement is shown in Fig 2.5b. It should be remembered that this strong agreement was reached without having to account for the effect of hBN birefringence on non-normal incident light.

Using the best fits to measured reflectivity, optical conductivity spectra are shown as a function of gate voltage. In Fig. 2.5c, splitting energy of the high-energy, and low-energy exciton-trion resonance peaks are plotted as a function

of gate voltage. The linear trend between gate voltage and peak splitting is anticipated by the many-body trion model [22], and cannot be explained by models that do not treat trions as a many-body system [11, 44, 10, 47]. Since the many-body trion model provides one measure of sheet charge density, whereas treating the device as an ideal MOS capacitor provides another, a comparison of these two metrics could be used to determine device ideality. Such a comparison is useful, because if the sheet charge density experimentally measured is much lower than the density of an ideal device, it could point to Fermi level pinning and exciton localization in the device [15].

The gate-controlled device can be simply understood as a MOS capacitor in accumulation mode, so a linear relationship should exist between sheet charge density and gate voltage. The capacitance per area of the device is equal to the dielectric capacitance per area, and is constant [56]. Carrier density and Fermi level of monolayer MoSe₂ are related by the simple Sommerfeld Model expression [55], but with the electron mass modified to $0.7m_e$. So, Fermi level and exciton-trion peak splitting are linearly dependent. Furthermore, according to the many-body trion theory [22], Fermi level and exciton-trion peak separation should be equal when Fermi level is above ~ 10 meV. The fits suggest that going from +2V to -22V increases the monolayer sheet charge density from 10^{11}cm^{-2} to $2.3 * 10^{12} \text{cm}^{-2}$. On the other hand, the MOS-capacitor model suggests that $6 * 10^{12} \text{cm}^{-2}$ carriers should have been introduced due to a -24 V negative bias (since +2V is assumed to be the charge-neutral point). Then, it can be concluded that the device under investigation has an ideality factor of about 40%, comparable to other gate-controlled trion spectroscopy measurements [Tony Heinz WS2 paper]. In the case that the discrepancy is due to lateral capacitances that were ignored, the device could be considered to have not suffered the effects of exci-

ton localization. However, a definite conclusion could not be drawn despite the high ideality factor.

CHAPTER 3
**REALIZATION OF EXCITON-TRION-POLARITONS IN HYBRID
PHOTONIC-2D MATERIAL SYSTEMS**

Optical conductivity calculated in Chapter 2 is perfectly adequate for explaining how exciton-trion superposition states respond to light in the linear regime. Because the encapsulated devices have very little photon confinement, photons in the system do not coherently interact with exciton-trion superposition states. How then, will the coherent interaction between photons, excitons, and trions occur? Will this trio of particles form a coherent polariton? What is the nature of these polaritons, if they do form? Experiments that will be discussed in this section, where exciton-trion-polariton dispersion will be measured, set out to answer these questions.

3.1 One-Dimensional Photonic Crystals as a Means of Inducing Strong Optical Coupling

In order to realize exciton-trion-polaritons, the toughest experimental question to answer is to find a medium in which photons can be confined; this, while maintaining high-quality exciton-trion superposition states. Typically, the most straightforward choice for realizing exciton-polaritons is a one-dimensional distributed Bragg reflector (DBR) [64] crystal, into which a half-wavelength defect mode is introduced. When the dielectric mirrors surrounding the defect are high-quality, a confined mode with large electric fields [64, 46, 58] is seen. It is this large electric field that can be assumed to strongly interact with excitons, or other matter resonances and form polaritons [75, 52, 41].

Such a cavity structure had already been realized in order to observe GaAs charged exciton-polaritons [59], and was recently realized for TMD polaritons [64]. These results will be discussed in the Discussion and Outlook section of the thesis. Instead, work discussed in this chapter focused on a different photonic crystal, which was initially explored in a recent experiment [43]. In this system, evanescent waveguide modes provided strong optical coupling to excitons in TMDs. As can be seen from the basic layout in Fig [Y1]a, the top half of the structure can be used for further dry-transfer and fabrication. So, this is an excellent choice for a system where a good balance between strong optical coupling and decent exciton-trion superposition states can be struck, as desired.

3.1.1 Design of 1D Photonic Crystals

The photonic crystal used that enabled strong optical coupling regime to be reached without compromising on monolayer MoSe₂ quality is a second-order diffraction grating, shown diagrammatically with a monolayer MoSe₂ suspended over it in Fig 3.1a. The unit cell of the photonic crystal, shown to scale, highlighted in blue in Fig 3.1c, is comprised of a trench of about 100 nm periodically etched with a period of $\Lambda = 510\text{nm}$ in the x direction, and is symmetric along z .

When the electric field of the incident light is TE-polarized, the second order grating folds waveguide modes with momentum $(2\pi/\Lambda)\hat{k}_x$ back to the Brillouin zone, back into the light cone. Thus, waveguide modes of the PC are allowed to radiate back out to free space [Welch 1989]. Simulations using Rigorously-Coupled Wave Analysis (RCWA) [Gaylord], and Finite-Difference Frequency

Domain [Zhao 2002] were utilized to find the grating period, trench width and depth. These simulations were done for the unloaded waveguide, and the mode near $k_x = k_z = 0$ was tuned to be nearly resonant with the lower exciton-trion superposition state. Results of the simulation [Okan ETP] are shown in Fig 3.1b, where the bands in blue are TE-polarized modes, with the chosen TE-polarized mode shown with increased weight. Fig 3.1c shows unit cell with the suspended monolayer. The color contrast shows the normalized electric field profile of the waveguide mode at $k_x = k_z = 0$. Decent overlap between the waveguide mode and the monolayer can be seen here. The more this overlap factor is increased, the stronger light-matter coupling will be observed. Strategies on how to further optimize this overlap function will be expanded on in Chapter 4. Another important factor of photonic crystals, quality-factor, will be measured in subsequent chapters.

One final parameter in designing the photonic crystal is the surface on which the monolayer MoSe₂ will be dry-transferred. As covered in previous Chapters, the grating surface should be quite pristine to minimize detrimental effects of disorder on the monolayer. Another concern is due to the fact that the monolayer is, in effect, being suspended on the photonic crystal. In transferring the suspended monolayer, it is critical to avoid any structural failures that would cause parts of the monolayer to crash into the grating trenches. This consideration is why the pitch of the photonic crystal trenches are kept relatively small. However, transferring a near-perfect, disorder free monolayer of MoSe₂ is still a serious challenge. Remarkable improvement of monolayer MoSe₂ PL lifetimes has been seen due to minimization of disorder in encapsulated TMD devices. [Ajayi]

3.1.2 Fabrication of 1D Photonic Crystals

To realize the 1D photonic crystals, a 1145 nm thick layer of SiO₂ was grown on a single-side polished, cleaned, slightly n-doped Si wafer via wet-chlorinated thermal oxide growth in a furnace at 1000 °C. A 125 nm thick stoichiometric Si₃N₄ layer was then deposited using a low-pressure chemical vapor deposition furnace process. Layer thicknesses and refractive indices were measured using an ellipsometer, and found to be 1.46 and 2.00 at 632 nm for SiO₂ and Si₃N₄, respectively. For the gratings in this chapter, photoresist was used with electron-beam (E-Beam) lithography to define and etch the second-order grating structure into the nitride layer. Below, process steps to spin, pattern and etch the photonic crystal structures will be covered:

Table 3.1: PMMA-Based Grating Fabrication Recipe

| Step | Description | Details |
|------|-------------|---|
| 1 | Spin | 4000 RPM, 2000 RPM/s acc, 60s |
| 2 | Softbake | 170 °C on Hot Plate, 600s |
| 3 | Spin | ESpacer 3000 RPM, 1000 RPM/s acc, 60 s |
| 4 | Expose | JEOL 9500 |
| 5 | Clean | DI Water, 2x {10 s Rinse + Blow-Dry} |
| 6 | Develop | MIBK:IPA 1:1, 2 minutes |
| 7 | Clean | First immersed in, then rinsed with IPA; blow-dried |

Once devices were patterned, a plasma reactive-ion etching (RIE) process was used to transfer the grating pattern onto the nitride substrate. Before any etch process, a 15-minute oxygen-plasma clean step was implemented. Then, the chamber was run empty for 5 minutes to season it. A blank wafer was run in the chamber, with Filmetrics measurements before and after etching to characterize etch rate. Finally, the etcher was run for the duration that would etch about 60 nm into the nitride. Afterwards, the devices were left overnight in

1165 solution. If the resist residue was still not removed, a further sonication step was taken. The solution was rinsed off with acetone, IPA, and blow-dried nitrogen successively. After fabrication was complete, the gratings looked like Fig 3.2a. Brightly colored, areas on the dark substrate are the photonic crystals, which can be seen by naked eye. Cleaned gratings were dry-transferred with a large MoSe₂ monolayer, as described previously. A common surface cleaning technique, oxygen plasma cleaning, was not employed during the fabrication process, in order to avoid exciton broadening due to disorder within dry-transferred MoSe₂ monolayers [50]. After dry-transfer was finished, large-area MoSe₂ monolayers, such as the one seen in the cross-polarized microscope image shown in Fig 3.2b, were fabricated. Unfortunately, the samples are not free of disorder. Furthermore, even in pristine areas of the monolayer, a slight change in monolayer reflectivity contrast hints that the sample doping may not be uniform, either. So, the experimental setup discussed in the next section has to be capable of dispersion measurements from a small, confocal area where effects of disorder are reduced.

3.2 Experimental Setup for Momentum-Space Dispersion Measurements

After a few modifications, a standard low-temperature confocal microscopy setup should be more than adequate to measure momentum-space dispersion from a small area. Details in setup design affect quality of measurements, and hence the accuracy of the subsequent theoretical analysis. Some of these details are discussed in the next paragraph.

Dispersion measurements for exciton-trion-polaritons are all based on reflection spectroscopy. Like the confocal, spatially-resolved optical conductivity measurements of Chapter 2, the basis of high-quality dispersion measurements starts by establishing a well-aligned optical axis, exactly in the same fashion as what was discussed in Chapter 2. Once the optical axis is established, the setup looks like Fig 3.3a. A 400 μm diameter, multimode fiber was coupled into the fiber collimator. The diameter of the collimated white light exceeded that of the objective back aperture, ensuring the full numerical aperture of the objective was utilized. Collimated white light was filtered by a long-pass filter with 600 nm wavelength (2 eV); removing most of the white light that was above the optical bandgap of the MoSe_2 monolayer, which is reported to be around 2.18 eV [3]. Then, the white light was polarized either along the x-axis, or along the z-axis. Following the beam-splitter, the light was focused down to a diameter of about $\sim 100\mu\text{m}$ using a 20x, 0.6 numerical aperture objective. Light coming back from the sample was collimated by the objective, had its polarization selected, and was focused onto the pinhole. When the two-polarizers were cross-polarized, rejection ratio at the collection side was greater than 100. Following the pinhole, the light was collimated, but was not focused onto the monochromator slit. Instead, the monochromator input slit was used as an aperture filter to select the $k_x = 0$ slice of the back-focal plane. This slice sent into the spectrometer, and imaged on the CCD. Thus, the image formed on the CCD array had wavelength information on the horizontal axis, and photon momentum information on the vertical axis. However, mathematical transformations needed to convert pixel to wavelength, or pixel to photon momentum are not straightforward, and are covered in detail in the Appendix. PL and reflection measurements are aligned optimally at the same configuration.

Like optical conductivity measurements discussed earlier, quantitative analysis of dispersion is made possible by normalizing the measurements. Fig 3.3b, along with a top-down look of the photonic crystal, shows how the various normalization schemes that will be used in this Chapter are done. Here, the pink circles represent the extent of the spatially-filtered light being collected by the setup. For instance, area (1), when light is TE-polarized, will show the photonic crystal dispersion, while (3) will have no dispersion features. \vec{E} denotes polarization of the white light in both the excitation and collection side.

3.2.1 Measurement and Analysis of Bare Waveguide Mode

Dispersion

The last step of building and characterizing the setup is by obtaining bare waveguide dispersion and analyzing it. These measurements can be used as a "gold-standard" of setup alignment quality. Once the E-Beam lithography process is confirmed to be working independently, say, via Scanning Electron Microscopy, the bare grating pattern then becomes a high-contrast feature with a known dispersion. Furthermore, the contrast of the dispersion measurement obtained in this system informs the contrast of any further measurements. Usually, if contrast in this step is inexplicably low, it points to a major misalignment of the confocal microscopy setup. If not fixed, these systematic errors will plague any further measurements; and prevent high-quality results that can be analyzed to a high degree of accuracy. Furthermore, quantitative analysis of the waveguide structure via FDFD is necessary in order to correctly analyze the dispersion of the coupled exciton-trion-polariton system.

Results of the bare waveguide dispersion is given in Fig 3.4a. Here, the right-hand side of the dispersion curve is the measured data, while the left-hand side is the results of an FDFD analysis [79], where the same normalization scheme as that illustrated in Fig 3.4b is used. Remarkable agreement of the measured and simulated dispersion spectra, strong qualitative agreement between the resonance lineshapes, along with relatively good agreement in absolute intensities imply that the setup is ready. Also, a quality-factor (Q-factor) of the grating can be found to be ~ 135 .

3.3 Exciton-Trion-Polaritons in Hybrid Photonic-2D Material Systems

With the setup optimization and characterization complete, dispersion of exciton-trion-polaritons can finally be investigated. As previously discussed in Chapter 1, the measured reflectivity could be used to determine light-matter coupling strength using the photon Green's function:

$$\begin{aligned} G^{ph}(\vec{Q}, \omega) &= \frac{1}{\hbar\omega - \hbar\omega_{PC}(\vec{Q}) + i\gamma_{PC} - \Sigma^{ph}(\vec{Q}, \omega)} \\ \Sigma^{ph}(\vec{Q}, \omega) &= -i\hbar \frac{|\xi(z_{ML})|^2}{2 \langle \epsilon \rangle} \sigma_{2D}(\vec{Q}, \omega) \end{aligned} \quad (3.1)$$

In a strongly-coupled system, both the optical conductivity $\sigma_{2D}(\vec{Q}, \omega)$ and overlap factor $|\xi(z_{ML})|^2$ are non-trivial, and cannot be independently solved for using a single dispersion measurement. In other words, simply measuring a strongly-coupled system will only provide $\Sigma^{ph}(\vec{Q}, \omega)$, which combines the opti-

cal conductivity (due to Coulomb interactions) as well as a mode overlap factor, which determines the photon-exciton coupling strength (according to Rana et al.'s model [58]). If an in-situ measurement of optical conductivity could be made, the optical coupling strength ceases to become a fitting parameter. In Finite-Difference Frequency-Domain (FDFD) analysis of measured dispersion, light matter coupling only depends on the absolute optical conductivity magnitude, which in turn depends on the interband velocity term [22]. Since the independently-measured optical conductivity already contains the interband velocity term, the entire agreement between measurement and fits have to be self-consistent. This self-consistent analysis serves as a complete semiclassical electrodynamic test of the Rana et al.'s model. The requirement for in-situ measurements is due to TMD disorder, which affects optical conductivity as a function of position. The next section discusses how this independent, in-situ, in-loco measurement of optical conductivity was realized.

3.3.1 In-Situ Optical Characterization of Monolayer MoSe₂ Optical Conductivity

In practice, it can be challenging to extract optical conductivity in a strongly-optically-coupled system. In typical, DBR-based polariton cavities, this would be a serious issue since every part of the device is strongly-coupled to the cavity mode. However, for the grating-based photonic crystal, having the electric field of the incoming white light perpendicular to the TE-polarization (along the x-direction in Fig 3.4b) results in minimal coupling. This can be understood better by referring back to Fig 3.1a, where the polarization orientation of TE-

and TM-polarized modes are shown. TE-polarized modes extend along the z-direction, while TM-polarized modes roughly extend out-of-plane. Then, a normalized reflectance measurement with light polarized along the x-direction would couple to none of the PC modes near exciton-trion resonances, and is an excellent approximation of the weak coupling regime where optical conductivity measurements approximate the ideal. Another consideration is steady-state photo-doping [48] of TMDs under large optical excitation densities. To minimize this second effect, incoming white light was spectrally filtered to be entirely below the bandgap of MoSe₂, and the optical power density was kept below 100 nW/μm².

Normalized reflectance measurement results used to extract optical conductivity are shown in Fig 3.5a, while the normalization scheme used to reach this result is shown in Fig 3.5b. In order to find the in-situ optical conductivity of the monolayer, area (2) measurements were normalized to area (1). Data was measured using Fourier-microscopy, and the vicinity of $k_z = k_x = 0$ was averaged to find the measured reflectance. The normalization scheme used here is very non-standard, and deserves a short explanation. Due to the dielectric thicknesses chosen, a reflection maximum occurs near the exciton-trion superposition states. The presence of this background maximum is not strongly affected by the presence of the monolayer; which dramatically reduces reflectance contrast due to exciton-trion superposition states. The reduced contrast pushes the lower exciton-trion superposition optical reflectance contrast below the typical 5% limit where steady-state is reliable; making it impossible to determine exciton-trion superposition peak splitting energy. To regain optical contrast due to exciton-trion superposition states, it has been empirically determined that normalizing the loaded waveguide reflectivity spectrum to an identical, but un-

loaded waveguide reflectivity works best.

As it can be seen in Fig 3.5a, two distinct resonance features appear in the measured reflectance spectra, shown in red. After the measurements were done, FDFD simulations were employed to generate the simulated normalized spectrum. In generating the simulated spectrum, the optical conductivity theory previously published by the authors [Rana Trions] was used. Fitting parameters for optical conductivity were only the carrier density and bandgap. For the optical conductivity curve shown in green, the normalized simulated reflectance curve shown in blue was generated. Remarkable agreement between measured and simulated data indicates that the optical conductivity theory [Rana Trions] previously verified in Chapter 2 works remarkably well for the device under discussion here.

From the optical conductivity spectrum, it can be found that the sample is n-doped with a carrier density of $n = 2.8 \times 10^{12} \text{ cm}^{-2}$. The Fermi energy of the sample is, then, 10 meV into the conduction band. According to [Rana ETP], Coulomb coupling of this system should be significant enough to form coherent exciton-trion-photon superposition states; namely, exciton-trion-polaritons.

3.3.2 Dispersion of Exciton-Trion-Polaritons

With the optical conductivity and bare waveguide dispersion known, exciton-trion-polaritons can be quantitatively investigated. By adding a thin, (0.7 nm [20]) conductive layer over the photonic crystal unit cell, FDFD simulations of the coupled system is made possible. The conductive layer simply uses the optical conductivity spectrum extracted from measurements described in the

previous Subsection. The right-hand side of Fig. 3.6a shows the measured dispersion, while the left hand side shows FDFD-based theory fits. The normalization scheme used by both measurements is shown on Fig. 3.6b. At first glance, remarkable agreement between measurement and theory can be seen. Three positive-mass polariton bands are seen, with clear bandgaps formed between the polariton bands due to Rabi splitting; denoted as lower (LP), middle (MP), and upper (UP) polariton bands. The Rabi splitting between LP and MP bands is 14 meV, while the MP-UP splitting is 31 meV. Both of these are larger than the photon lifetime of ~ 11 meV; confirming that the entire system is in the strong-coupling regime.

All of the observations above are consistent with theoretical expectations of exciton-trion-polaritons [Rana ETP]. Furthermore, the precise, self-consistent agreement between theory and experiment strongly suggests that exciton-trion-polariton theory [Rana ETP] uniquely explains almost all of the experimental observations. This implies coherent superposition states of excitons, trions, and photons emerge readily in systems. This realization is quite profound, and its potential impact to optoelectronic device design will be further discussed in the Discussion section.

3.3.3 Dispersion of Exciton-Trion-Polaritons via Photoluminescence

Dispersion measurements of exciton-trion-polaritons can be done not only by reflection, but also by PL. To do so, an optical excitation of the monolayer sample above the bandgap should suffice. Some of the excited excitons and trions

will couple to the photonic crystal and form exciton-trion-polariton states before radiating out to free space. Configuration of the setup is shown in Fig 3.7b. Instead of white light excitation, a pump laser with $200 \mu\text{W}$ intensity was focused onto an area of $\sim 5\mu\text{m}$ radius (the green spot on the ML in Fig 3.7). The laser was filtered on the collection side, and the emitted photoluminescence dispersion was measured. Polarization of the pump laser was not found to affect the dispersion, so a linear polarization with the maximum external quantum efficiency was chosen.

Resulting spectra is shown on the left-hand side of Fig 3.7a, with photon density-of-states (PDOS) used as theory. While qualitative agreement is again quite strong, especially around the LP-MP bandgap, some major differences between measurement and theory can be seen. However, these differences turn out to be fairly benign. The first is a slight redshift of the measured PL spectrum. This, simply, is an effect of laser heating. Temperature-dependent PL measurements of the monolayer in the weak-coupling regime (Fig. 3.7c) show this temperature-dependent redshift. Secondly, the spectral weights of the measured polariton bands are remarkably different than the PDOS spectral weights. While this is not completely understood, one possible explanation emerges from the PDOS being more closely related to the absorption, whereas the PL dispersion that is observed is due not only to absorption, but also to carrier dynamics. While radiative dynamics of exciton-trion states [57] have been investigated previously, no attempt has been made here to explain the discrepancies using carrier dynamics analysis. How the exciton-trion-polariton system evolves, and maintains coherence, are open questions with a few works being dedicated to it already [70].

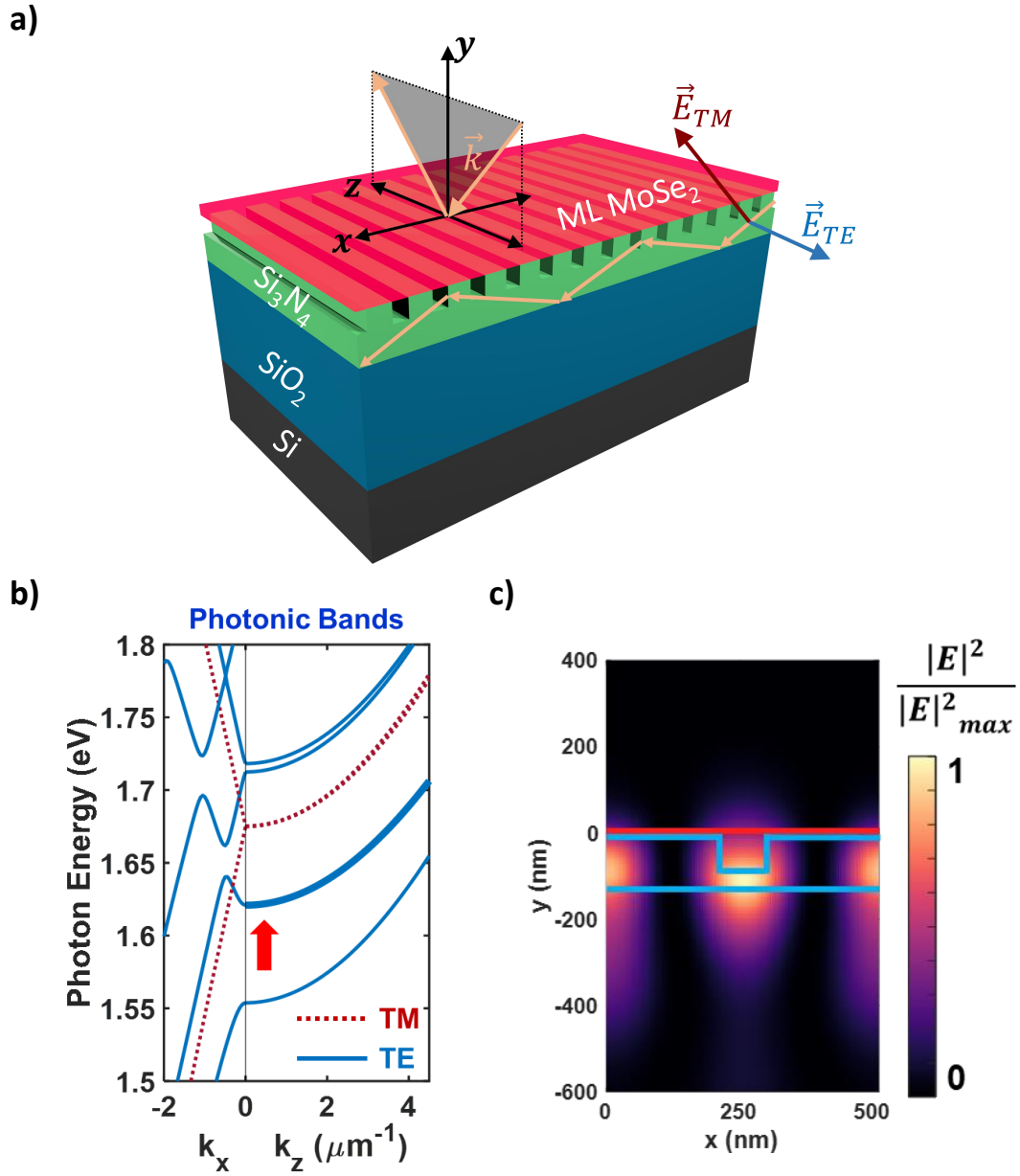


Figure 3.1: Hybrid photonic crystal-monolayer MoSe₂ device used to realize exciton-trion-polariton dispersion. a. 3D diagram of the device. For an incoming plane wave of momentum \vec{k} , the TE-polarization shown in blue couples to the PC modes. Due to the large photonic crystal momentum, the TM-modes are almost along the y axis, so any optical excitation in the experiment discussed in this chapter could excite TM-modes. b. Band structure of the photonic crystal across \vec{k}_x and \vec{k}_z directions for TE- and TM-modes. The heavier blue band is used for exciton-trion-polariton dispersion measurements. The approximate energy of the lower exciton-trion resonance is indicated by the large red arrow. c. Normalized electric field intensity distribution across one period of the photonic crystal at $\vec{k}_z = \vec{k}_x = 0$ for the highlighted TE-mode. Imperfect, but decent mode overlap of the waveguide mode with the monolayer is found.

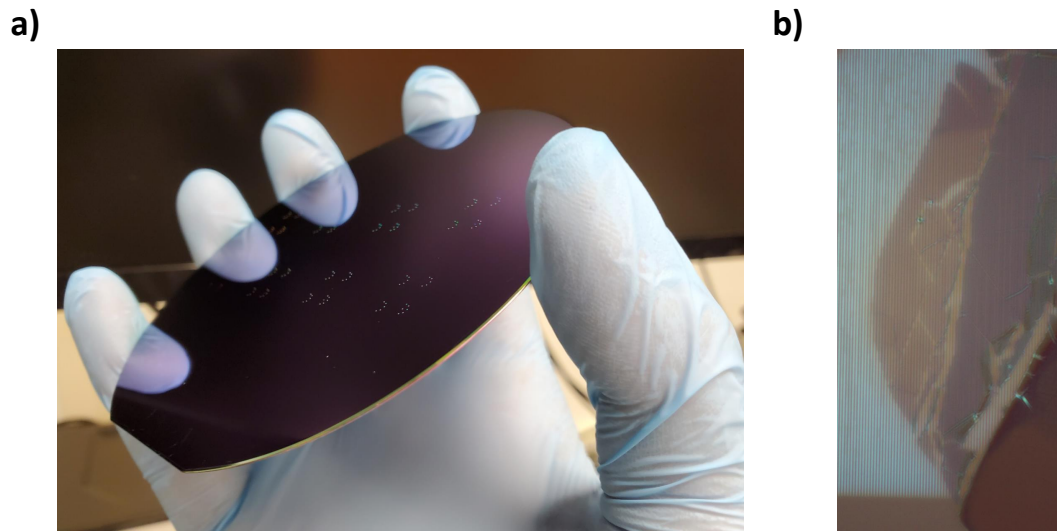


Figure 3.2: a. Photo of fabricated grating structure, due to diffraction, semi-circles brightly colored in green and other hues can be seen. These sharp colors could be used as a quick sanity-check of grating quality before quantitative measurements begin. b. Microscope image of device used in measurements discussed in this Chapter. The blue areas are that of the grating, and is caused by the cross-polarization technique used in obtaining the microscope image. The light gray area in the center is the monolayer MoSe₂ flake. It can be seen that large cracks, and other disorder is present. However, large areas of the sample were not affected (at scales resolvable by visible wavelengths) by disorder. An astute observer might notice that the top of the flake is darker than the center. This is believed to be due to carrier density variations of the monolayer flake. However, short of a large-area, broadband, in-situ spectroscopy measurement, this belief could not be verified.

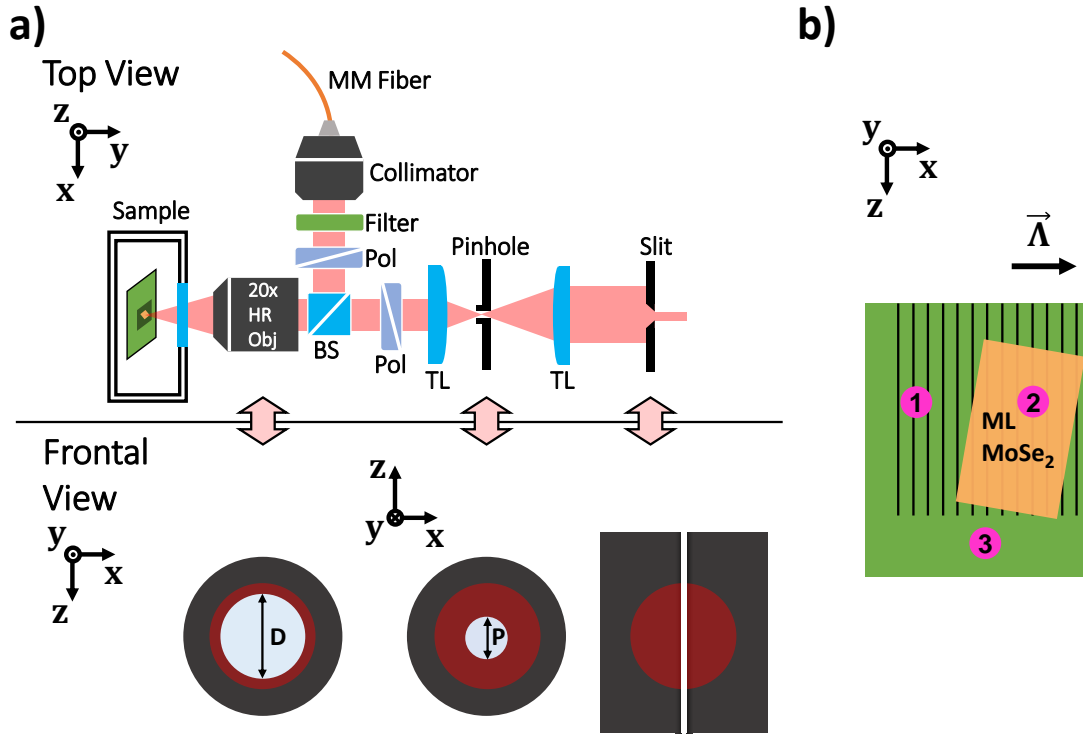


Figure 3.3: Setup and measurement summary a. Diagram of the setup looking from the top, and head-on. 532 nm laser used for alignment and PL not shown. White light exits the multimode fiber, is collimated, color-filtered, polarized, and sent into the microscope. The frontal view of the objective shows that the collimated white light diameter is slightly larger than the back-focal plane diameter (D), ensuring the full numerical aperture of the objective is utilized. The frontal view of the pinhole shows how the pinhole spatially filters a small diameter (P) of white light. P was magnified to $\sim 10\mu\text{m}$ on the image plane. Head-on view of the slit shows how only the immediate vicinity of $k_x = 0$ is selected for dispersion measurements. The diameter of this slit simultaneously sets the frequency and momentum resolution of the setup. Appropriate choice of collimator and high-resolution objective played a significant role in ensuring high-quality, artifact free dispersion measurements. b. Three different measurements whose effective collection area are highlighted in pink are shown. (1), (2), and (3) correspond to the bare waveguide, loaded waveguide, and unpatterned substrate, respectively. All measurements in this Chapter, unless states otherwise, were done at 20 K.

a) Unloaded Waveguide b)
Reflection Spectra
(TE-Polarized)

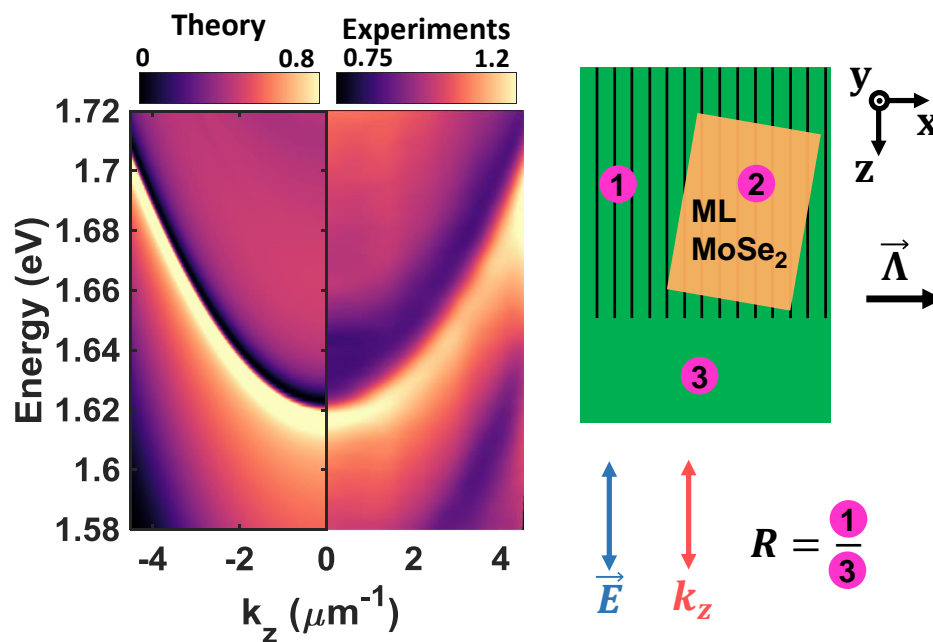


Figure 3.4: Unloaded waveguide dispersion. a. Right-hand side: Unloaded waveguide dispersion measured via normalized reflectivity. Left-hand side: FDFD Fit to the measured dispersion. FDFD was normalized in the same manner as the measurements. Remarkable agreement between theory and measurement can be seen. b. Scheme to obtain normalized reflectivity. Numbered pink areas denote the locations on the sample where each measurement was taken. Unloaded waveguide dispersion measurements normalized 1 by 3. Electric field, and dispersion measurement direction were both along the z-axis.

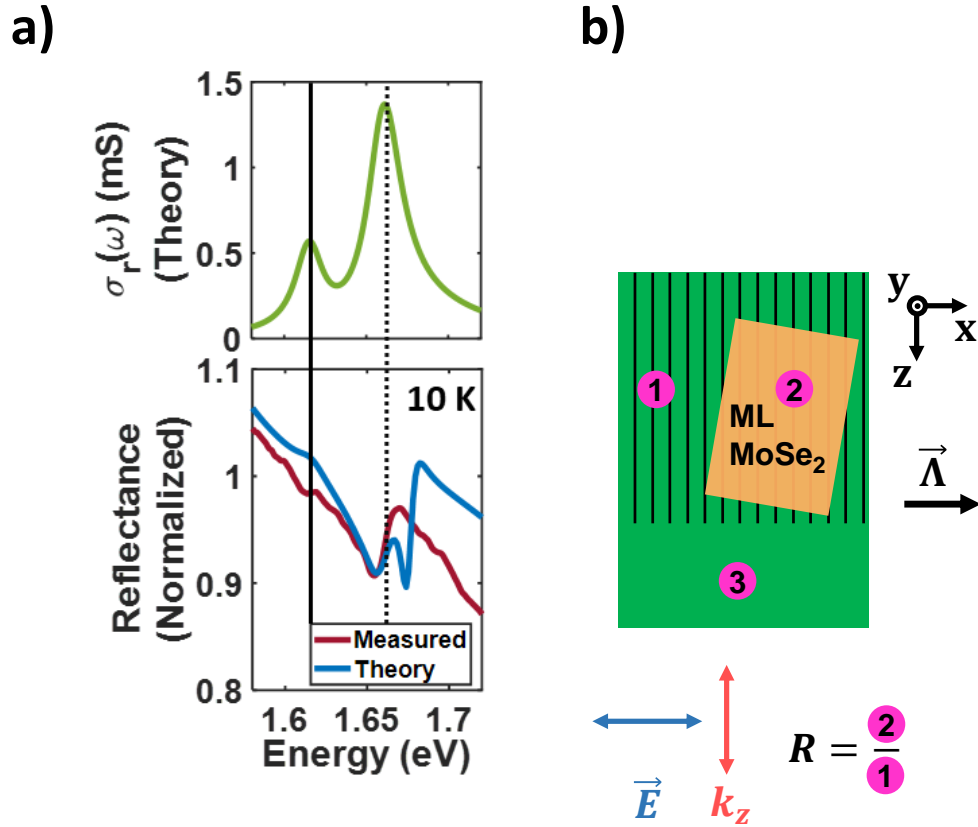


Figure 3.5: Determining in-situ optical conductivity of the monolayer MoSe₂ flake. a. Top; optical conductivity model generated from [22]. Bottom; measured normalized reflectivity spectra and theory fits showing strong agreement. Measurements were obtained via dispersive measurements, and only the zero-momentum area was averaged. FDFD fits were normalized and momentum-space filtered in exactly the same fashion as the measurements. FDFD fits used the optical conductivity shown on the top side. b. Measurement scheme. Area 2 was normalized by Area 1. Dispersion measurements were along z-axis, but only a small region around zero-momentum was averaged to generate curves in (a). Electric field of incoming white light was polarized along the x-direction. This polarization strongly couples to neither TE-, nor TM-polarized PC modes.

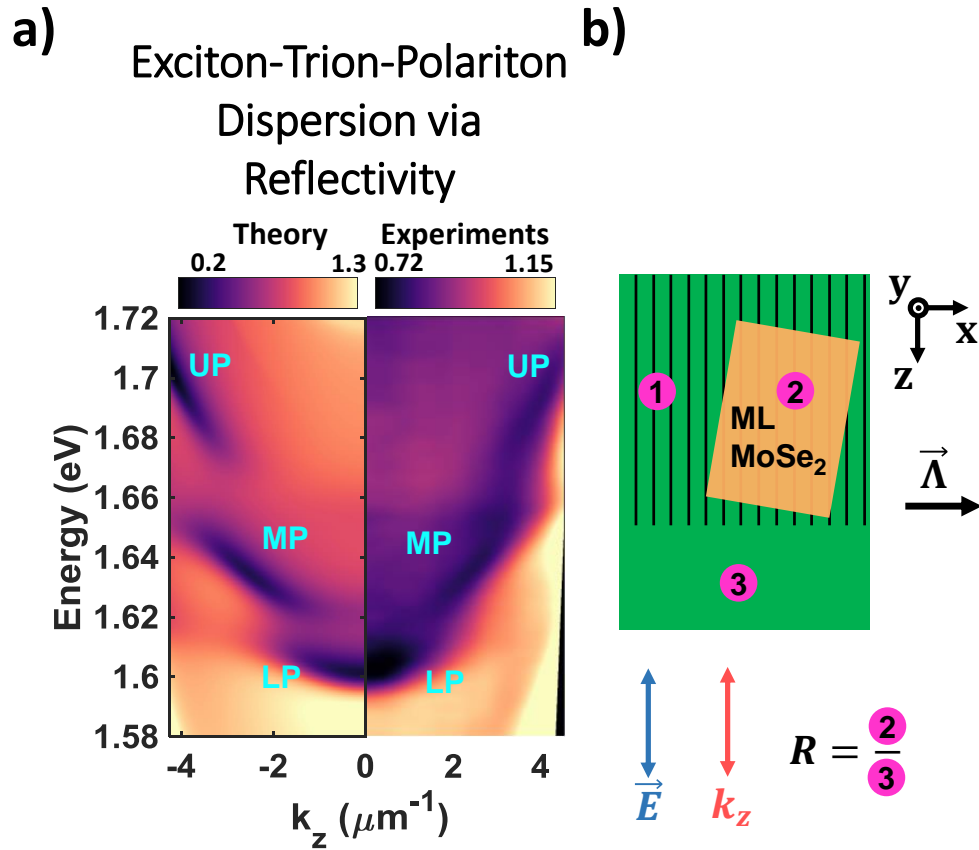


Figure 3.6: Exciton-trion-polariton dispersion via normalized reflectivity. a. Comparison of measured (right-hand side) and theoretical (left-hand side) dispersions of exciton-trion-polaritons. Remarkable quantitative agreement between theory and measurements can be seen. Both results have three Rabi-split positive-mass polariton bands; denoted lower (LP), middle (MP), and upper (UP) polariton bands. Slight quantitative disagreements between measured, and theory dispersions is attributed to disorder in the photonic crystal structure b. Measurement scheme for normalized reflectivity. Numbered pink areas denote the locations on the sample where each measurement was taken. Unloaded waveguide dispersion measurements normalized 1 by 3. Electric field, and dispersion measurement direction were both along the z-axis.

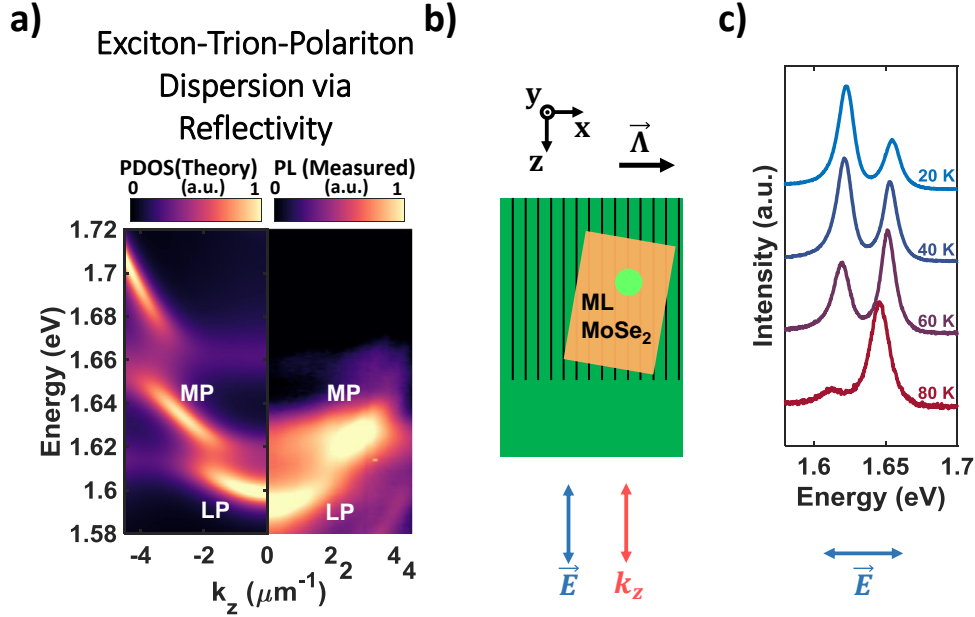


Figure 3.7: Exciton-trion-polariton dispersion via photoluminescence. a. Comparison of measurement (right-hand side) and theory (left-hand side). Theory curves were generated by photon density of states, calculated via the Green's function method. Reasonable agreement can be seen between the two curves; and disagreements are elaborated on (c) b. Measurement scheme. A 532 nm, continuous-wave laser was used to photo-excite carriers, resulting in PL emission. Dispersion of the PL was obtained along the z-axis. PL emission was linearly polarized along the z-axis. Dispersion was seen not to depend strongly on pump polarization, which was always linear. c. Temperature-dependence of PL from the MoSe₂ monolayer, in the weak-optical-coupling regime. A redshift of the upper and lower exciton-trion resonances can be seen, while the splitting energy between the bands were not found to depend strongly on temperature. This redshift partly explains why the LP band is significantly redshifted; sample heating due to the relatively high fluences used in the PL measurement tuned the lower E-T superposition state closer to the bottom of the PC mode, increasing the LP-MP splitting. The upper polariton band seen in theory curves is almost missing from measurements. This could be explained by the lower E-T having much larger PL emission spectral weight due to the incoherent relaxation from the upper E-T resonance to the lower one before photoemission [57].

CHAPTER 4
CONTROLLING EXCITON-TRION-POLARITON DISPERSION BY
TUNING CARRIER DENSITY

The remarkable agreement seen in the previous chapter between experiments done on hybrid 1D photonic crystal-2D TMD systems and exciton-trion-polariton theory demonstrates a system in which optical properties can be remarkably altered by electronic means. The simplest way to realize this effect is by considering exciton-trion-polariton dispersion as a function of MoSe₂ monolayer carrier density.

A simple, qualitative description of the effect of increased carrier density on optical characteristics of exciton-trion-polaritons is illustrated in Fig 4.1. Carrier density of the MoSe₂ is increased from nearly intrinsic levels on the left-hand dispersion curve, to large carrier densities such as $5 \times 10^{12} \text{cm}^{-2}$ on the right-hand dispersion curve. Before a detailed discussion of these calculated dispersion measurements, it makes sense to explain the expression used to generate it:

$$R(\vec{Q}, \omega) = |1 + B * G(\vec{Q}, \omega)|^2 \quad (4.1)$$

Here, $G(\vec{Q}, \omega)$ is the photon Green's function previously found in Eq 3.1, and the exciton-trion optical conductivity is calculated in the same way as before. The plots shown in the figure are calculated exciton-trion-polariton dispersion as a function of monolayer doping. With increasing carrier density, two prominent features can be noticed. First, the strength of the LP-MP bandgap goes from nearly 0 to more than 10 meV. Second, dispersion of all three polariton bands change with increasing carrier density. The latter effect emerges due to exciton-

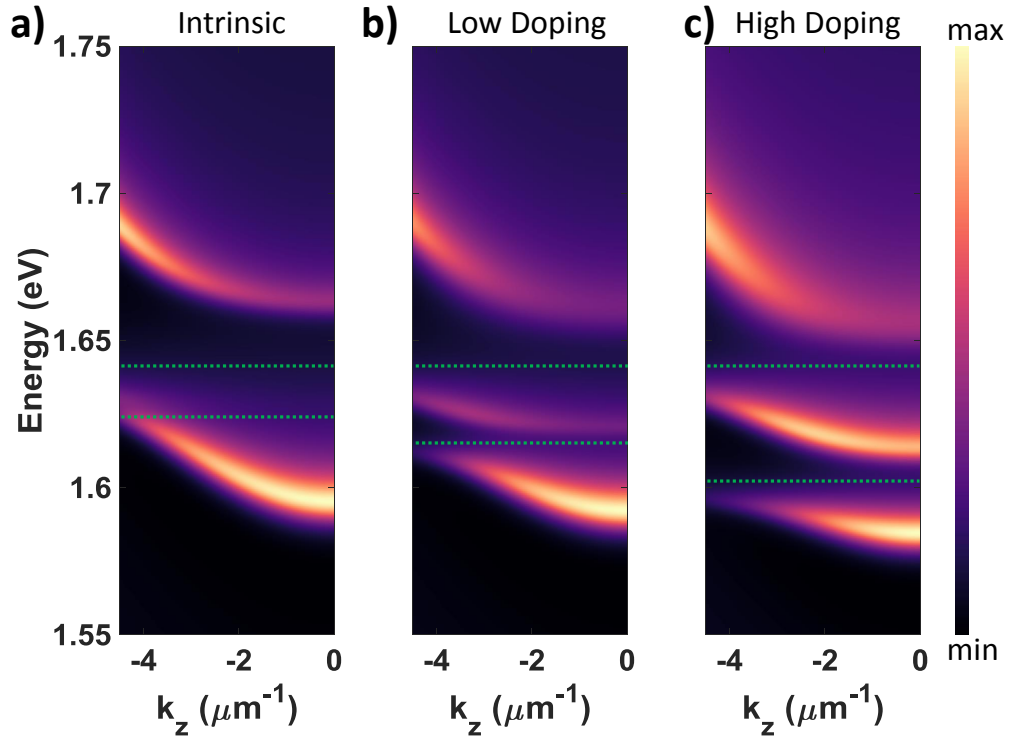


Figure 4.1: Simulated carrier-density control of exciton-trion-polaritons in an idealized, but practically-attainable device. a. Intrinsic, b. Small, and c. Large n-doping of the sample. For each curve, the upper and lower exciton-trion (E-T) superposition states are shown by dashed green lines. As carrier density is increased, the LP-MP polariton bandgap opens around the lower E-T superposition state, which is redshifted due to increased Coulomb coupling between excitons and trions. Remarkable changes to the reflectivity of the polariton device thus occurs as background carrier is modulated.

trion peak splitting, which in the graphs can be seen by the dashed green lines. According to the exciton-trion-polariton model [Rana ETP], both of these features should be apparent on any practically realized, carrier-density-controlled exciton-trion-polariton device.

The hybrid 1D photonic crystal-2D TMD monolayer serves as the ideal system whereby both of these hypotheses can be tested. However, some modifications to the fabrication procedure are required in order to introduce carrier-density control of the system.

4.1 Fabrication Considerations to Realize Simultaneous, Strong Optical and Coulomb Coupling in Exciton-Trion-Polaritons

4.1.1 Photonic Crystal Fabrication.

The first point to consider is the Si substrate doping. For the carrier-density controlled devices, Si doping was degenerately n-doped. For the device in Chapter 3, lightly n-doped substrates were used instead, since carrier density in the monolayer was determined by extrinsic doping and electrostatic doping via the substrate [25], and was not electrically controlled. In the case that one needs to control the carrier density, one of the contacts of a simple capacitor needs to be connected to the MoSe₂ monolayer, allowing it to accumulate charge along with the capacitor. This was done by choosing a degenerately-doped Si substrate to serve one of the contacts, while the other contact was simply a metal contact lithographically defined over exposed parts of the monolayer with the same methods as in Chapter 2. The degenerately n-doped substrate prevents any carrier freeze-out of the Si contact, ensuring monolayer carrier density is controlled even at cryogenic temperatures. Two details require attention to make sure these devices are successfully fabricated; first, oxidation reaction rates differ for heavily doped substrates [16], second, losses of the PC modes due to the substrate becomes a more serious concern. The first issue was solved simply by accounting for the growth rate change of oxides due to dopants.

To solve the second issue, the most straightforward solution is to simply grow a thicker oxide layer on the Si substrate. However, increasing the oxide thickness reduces the unit capacitance per area of the capacitor:

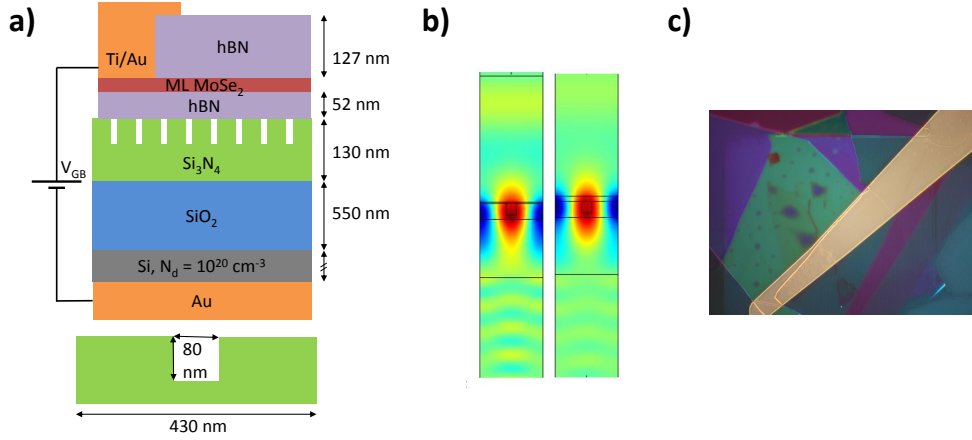


Figure 4.2: Modifications to exciton-trion-polariton device fabrication. a. Top, MOS-capacitor structure used to control carrier density of MoSe₂ monolayer. Bottom, photonic crystal unit cell. b. FDFD mode simulations of the PC mode with and without hBN. Left, PC mode profile for structure in (a). Mode overlap with Si can be clearly seen. Right, PC mode after added hBN on top of PC. Si loss is reduced, mode profile is higher; resulting in better overlap with monolayer MoSe₂ (not shown). c. Cross-polarized microscope image of fabricated sample. Yellow shade is the Ti/Au contact, while green area is hBN-encapsulated, with the darker green shade in the middle being the device. Circular perturbations to the structure are trapped air bubbles; causing disorder to both photonic and electronic degrees of freedom of the system.

$$C = \epsilon_o \left(\sum_i \frac{d_i}{\epsilon_i} \right)^{-1} \quad (4.2)$$

Where i denotes the stack of dielectric films that form the capacitor. So, to ensure that the Fermi level can be tuned sufficiently high, the substrate thickness needs to be kept low. Of course, charge can be accumulated further by increasing the voltage across the capacitor. However, the dielectric breakdown of the thin films comprising the capacitor limit the maximum voltage that can be applied across the device. Between these considerations, a SiO₂ substrate thickness of 550 nm can be found to offer a sound compromise; while losses from the substrate are not significant at this thickness, capacitances are sufficiently high as to allow the monolayer to be doped. The top part of Fig 4.2a shows the

resulting structure.

Fabrication of the photonic crystal is also worth revisiting. In the previous devices, a PMMA-based recipe was employed to fabricate the 1D grating. However, the electron dose required for the PMMA to clear is a very gradual function of electron dose [35]; providing low contrast for the grating structures and thus reducing Q-factor. Instead, ZEP520A could be used. Unlike PMMA, this resist's clearance threshold is a very sharp function of electron dose [35]; leading to high-contrast patterns on the resist that increase Q-factor. The modified recipe for grating fabrication is shown in Table 4.1, with the resulting PC unit cell shown on the bottom side of Fig 4.2a:

Table 4.1: ZEP520A-Based Grating Fabrication Recipe

| Step | Description | Details |
|------|-------------|---|
| 1 | Dilute | ZEP520A:Anisole 1:1 Volume |
| 2 | Spin | 4000 RPM, 2000 RPM/s acc, 60s |
| 3 | Softbake | 170 °C on Hot Plate, 180 s |
| 4 | Spin | DisCharge 3000 RPM, 1000 RPM/s acc, 60 s |
| 5 | Expose | JEOL 9500 |
| 6 | Clean | DI Water, 2x {10 s Rinse + Blow-Dry} |
| 7 | Develop | Amyl Acetate, 2 minutes |
| 8 | Clean | First immersed in, then rinsed with IPA; blow-dried |

4.1.2 hBN Encapsulation of Monolayer MoSe₂

Another venue of improvement comes from reducing disorder in the monolayer MoSe₂. Recent studies [50] has shown how encapsulating a TMD sample with hBN can lead to dramatic increases in optical lifetime. Such increases would result in an increase in exciton-trion-polariton lifetime, and hence, Q-factor. At the same time, the high dielectric constant of hBN significantly raises the spa-

tial profile of the PC modes. This can be seen in Fig 4.2b, which shows the TE-polarized PC mode electric field profile with and without hBN substrates directly over the grating. Furthermore, pulling the PC mode higher increases the overlap of it with the MoSe₂ monolayer; increasing the strength of optical coupling further. As an added benefit, oxygen plasma cleaning the substrate to minimize photonic disorder becomes possible when there is a ~ 50 nm to passivate dangling bonds that might have been generated by oxygen plasma cleaning [71].

Of course, adding the hBN layer is not without disadvantages. First, fabricating an encapsulated device requires three consecutive PDMS dry-transfer steps. Barring failures of the transfer step, wrinkles and bubbles (see Fig 4.2c) introduced between each layer due to stacking faults adds disorder to the TMD device. Presence of such disorder could be prohibitive in controlling the carrier density of the monolayer, as well as prevent lateral transport in the device. It is expected that implementing superior 2D material stacking techniques [Guimaraes 2D] will improve exciton-trion-polariton devices noticeably. In addition, placing an hBN layer over the PC changes its zero-momentum energy. Careful FDFD simulations that account for hBN's full anisotropic dielectric constant need to be performed in order to precisely make PC mode dispersion resonant with exciton-trion superposition states. Fortunately, extensive studies of exfoliated hBN flakes already exist [Rah 2019].

4.2 Electrical Control of Exciton-Trion-Polariton Dispersion

Based on these refinements, a new carrier-density-tunable exciton-trion-polariton devices was fabricated. The cross section of this device looked similar to Fig 4.2a. All thin film thicknesses, as previously discussed, were measured by thin film reflectance measurements and subsequent analysis. The device was glued onto the chip carrier; contacts were wire bonded; the chip was then mounted onto the cryostat. To demonstrate electrical control of exciton-trion-polariton dispersion, the following experimental procedure was used:

- Sample was left in a strong vacuum.
- Biasing circuit was connected the PCB; ESD and shock protection was ensured by PCB leads all being grounded until bias circuit was turned on.
- PCB-Sample connections were turned on, PCB ground latches were turned off.
- Liquid helium was transferred.
- Sample was cooled to 20 K at a rate less than 0.1 K/second. Temperature was kept unchanged until measurement concluded.
- Device voltage was brought to +100 V, and back to +50 V.
- Voltage was stepped from +50 V to -300 V. Voltage changes were done with 0.1 V/s rates, and 15 minutes were elapsed at each new voltage to ensure steady-state operation.
- White light was turned on, and the contact junction illuminated.
- Measurements were taken at new voltage after photocurrent transient due to white light illumination decayed.

Measurements were identical to those described in Chapter 3 except that dispersion was normalized via a Ti/Au mirror reflectance spectrum. Results are shown in Fig 4.3. For each curve, the right-hand side shows measurements, and the right hand side is the theory from Eqns. 4.1, and 3.1. Good agreement between measurements and theory suggests that the device behaves quite closely to what is expected from a carrier-density-controlled exciton-trion-polariton system with increasing background carrier density: An increase of LP-MP bandgap size and a decrease in MP-UP size as well as an increase in LP-MP and MP-UP gap energy splitting. The next paragraph provides an in-depth discussion of agreement and discrepancies between measurements and theory.

Top left, top right, bottom left, and bottom right measurements were done at a gate bias of +50 V, -5 V, -150 V, and -300 V, respectively. In all measurements, the high-contrast dispersive area ranging between 1.57 eV and 1.64 eV is the LP-MP complex. Instead, the UP band has fairly weak contrast both in measurements and simulations; and can be seen as the flat line around 1.64 eV. At +50V, the LP-MP bandgap is not open, but clearly opens by -5 V. As gate voltage is set to -5, -150 and -300V, the energy of the LP-MP bandgap redshifts from 1.619 eV, 1.615 eV, and 1.595 eV respectively. Also, the the LP-MP bandgap increases in size; demonstrating increasing coupling strength. Simultaneously, the MP-UP bandgap stays relatively constant, and the UP band oscillator strength decreases. On the other hand, the theory curves consistently underestimate LP-MP bandgap energies, while overestimating the MP-UP ones. Also, the measured MP dispersion has much higher curvature (in other words, lower effective mass,) than theory. Both of these effects likely stem from the optical conductivity model used in the fitting slightly overestimating the oscillator strength of the upper exciton-trion resonance, and underestimating the lower one. By adjust-

ing the trion binding energy parameter used in the optical conductivity model, which is a parameter that is hard to determine precisely by experiments, better agreement between experiment and theory could be reached.

In this device, the charge-neutral point, where the LP-MP bandgap is almost fully closed, is found to be around +50 V. With the ideal MOS-capacitor model, such a high bias voltage should not have become the charge-neutral point. This deviation from charge-neutrality is quite puzzling; as it is not seen for the top-hBN-encapsulated device discussed in Chapter 2. This is an important clue, as the one remarkable difference in the fabrication processes of the devices in Chapters 2 and 4 is how the hBN-encapsulation was done. For the device in Chapter 2, a pristine monolayer of MoSe₂ was exfoliated directly on SiO₂, and was quickly encapsulated with hBN. In this fabrication scheme, all of the interfaces in contact are pristine, and are not in contact with PDMS or other organic solvents; leading to a very pristine TMD interface. However, for the device discussed in this Chapter, the facet of bottom hBN on which the monolayer MoSe₂ is transferred is contaminated. Such contamination could locally dope the monolayer, how the Fermi level is affected by such variations is known to cause disorder [15]. Some experimental works where polymer residue contaminated the TMD-hBN interfaces have also suffered from serious deviations of their charge-neutral point [36, 70]. Identifying and mitigating such deviations from ideality are important for future device applications involving exciton-trion-polaritons, where transport of quasiparticles will play an increasing role [8]. Thus, a method of measuring device ideality in-situ would be desirable. The next Subsection discusses a possible way to calculate this metric.

4.2.1 Discussion on Device Ideality and Exciton Localization

A helpful metric of device ideality could be derived using a simple, MOS-capacitor model to estimate the electron density per unit area on the contacts. Then, it is possible to assume that the carrier density per unit area of the monolayer and contacts should be equal in steady-state. This provides a second metric for n_{ML} that can be compared to the extracted values from the monolayer using the model. The MOS-capacitor device in Fig. 4.2a was found to have a depletion threshold voltage of $V_t \simeq 100V$. Depletion capacitance of the device was much smaller than the dielectric capacitance [Chenming Hu notes], and was subsequently ignored. So, the carrier density of the monolayer can simply be estimated to be $n_{ML} \simeq C(V_G - V_{fb}) \simeq CV_G$. Then, the simplified capacitor model would not be able to predict the charge neutral point being at +50 V. This discrepancy could be due to lateral capacitances in the system that were ignored, or due to a transient electron density generated by the white light that was used in the dispersion measurement. To mitigate this issue, the formula was modified to $n_{ML} \simeq C(V_G - V_{neutral})$, where $V_{neutral}$ was the voltage where carrier density of the monolayer was extracted to be negligible.

Comparing the background carrier density of the monolayer estimated by this simplified model to values extracted from the exciton-trion-polariton dispersion fitting allows for an investigation of device ideality. Ignoring parasitic capacitances between the contact metal and the monolayer, the carrier density measurements should be equal using both calculations. In case of constant extracted carrier densities under increasing gate voltage bias, Fermi level at the measurement location could be pinned. Such Fermi level pinning localizes excitons, and could effect device mobility [15]. In these localized excitons, oscillator

strength transfer between exciton-trion superposition states would still be observed, but in the absence of peak energy shifts [AIP Proceedings Russians]. Instead, if the extracted carrier densities scale linearly with increasing gate voltage bias but not at the same rate, this could imply parasitic capacitances, possibly in the lateral dimensions of the device. In an ideal device, both methods should yield the same carrier density value.

Using the capacitance per area formula of Eq. 4.2, the capacitance per area of the structure in Fig. 4.2 was calculated as follows:

$$C = \epsilon_0 \left(\frac{d_{SiO_2}}{\epsilon_{SiO_2}} + \frac{d_{Si_3N_4} - d_{gr}}{\epsilon_{Si_3N_4}} + \frac{d_{gr}}{\eta(\epsilon_{Si_3N_4} - 1) + 1} + \frac{d_{hBN}}{\epsilon_{hBN}} \right)^{-1}$$

$$\simeq 50 \mu F / m^{-2}$$

Here, d_{SiO_2} , $d_{Si_3N_4}$, d_{hBN} correspond to thicknesses of the SiO_2 , Si_3N_4 , and hBN layers, respectively. ϵ values are DC dielectric permittivities of the same layers. d_{gr} is the thickness of the grating layer, where etched portions are assumed to be air. To calculate the average dielectric constant of this layer, the duty cycle η of the grating was used to average between the filled, and etched portions of the grating, resulting in a dielectric constant of $\epsilon_{gr} = \eta(\epsilon_{Si_3N_4} - 1) + 1$. Once the capacitance per area of the dielectric is calculated, it is possible to use

Table 4.2 compares the carrier densities found via the model (extracted) and are expected by the gate voltage (idealized). The linear dependence between extracted carrier density and voltage demonstrates that the Fermi level in the device was not pinned. Despite minimal efforts to optimize contact quality and a rather basic 2D material fabrication process that introduces disorder, an ideality factor of 40% was reached. With very basic improvements to 2D fabrication,

some of which will be discussed in the Appendix, nearly ideal devices could be obtained.

Table 4.2: Comparison of Extracted and Calculated Carrier Densities of Exciton-Trion-Polariton Device

| V_G (V) | Extracted Carrier Density [cm^{-2}] | Ideal Carrier Density [cm^{-2}] |
|-----------|--|--|
| +50 | $3 * 10^{11}$ | N/A |
| -5 | $1 * 10^{12}$ | $2 * 10^{12}$ |
| -150 | $2 * 10^{12}$ | $5 * 10^{12}$ |
| -300 | $4 * 10^{12}$ | $1 * 10^{13}$ |

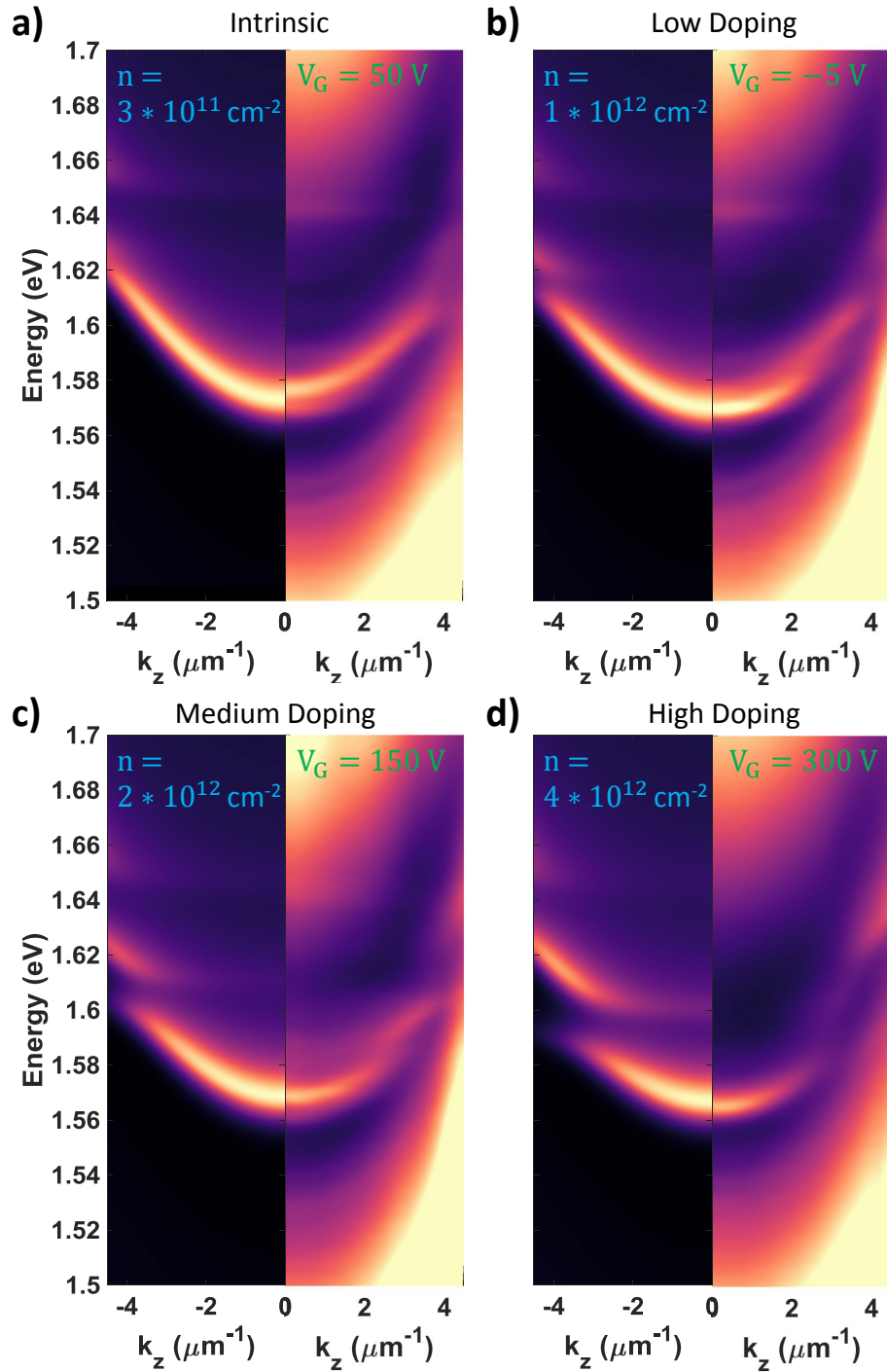


Figure 4.3: Carrier density dependence of exciton-trion-polariton dispersion. a. Dispersion with intrinsically-limited background carrier density. LP-MP bandgap appears almost fully closed. b. Dispersion with $n_e = 1 * 10^{12} \text{ cm}^{-2}$. The LP-MP bandgap opens at 1.618 eV, and $4 \mu\text{m}^{-1}$ c. Dispersion with $n_e = 2 * 10^{12} \text{ cm}^{-2}$. The LP-MP bandgap moves to 1.61 eV, and $3.8 \mu\text{m}^{-1}$ b. Dispersion with $n_e = 4 * 10^{12} \text{ cm}^{-2}$. The LP-MP bandgap further redshifts to 1.59 eV, and to $2.5 \mu\text{m}^{-1}$. This trend is consistent with ETP theory [58]

CHAPTER 5

DISCUSSION AND OUTLOOK

Besides its strong connections to the fundamental physics problems explored within the Fermi-polaron framework in cold atom [49] and condensed matter systems [60, 13], exciton-trion-polaritons also establish a platform wherein novel low-power linear, and nonlinear photonic device applications could potentially be realized.

It is possible to separate research into novel device technology into three phases: development of a correct theoretical framework; an experiment in which a system is built to verify this theory; control of the system to exploit novel abilities provided by the theory. In Chapter 1, a review of the various theories for trions were discussed. Profound challenges brought to the mainstream of trion theory [13, 60, 46], and the precise, complete picture that unified these perspectives by Rana et al. [58, 22, 57] motivated a push for careful spectroscopy that could confirm this theory's accuracy. Work shown in Chapters 2-4 consisted of such spectroscopy measurements. It is in this Chapter that the potential for device applications stemming from remarkable agreement between Chapter 1's theory, and Chapters 2-4's experiments will be discussed.

5.1 Potential Device Applications of Exciton-Trion-Polaritons

5.1.1 Low Power Optoelectronic, or All-Optical Modulators

Exciton-trion-polariton systems simultaneously possess strong Coulomb and optical coupling. Strong Coulomb-coupled exciton-trion superpositions result

in a giant change to optical conductivity in a narrow part of the spectrum. For applications restricted to this narrow-band, a relatively small change of carriers dramatically altering optical transmission around E-T resonances. For instance, consider the device in Fig 4.2. If the PC is designed in a way that a guided mode can couple incoming light at the E and k corresponding to a the LP-MP bandgap, then a carrier density change of $7 * 10^{11} \text{ cm}^{-2}$ is sufficient to make an electro-optic modulator with signal modulation depth of $\sim 10\%$ of the incoming signal. For a practical device with $5 \mu\text{m}$ diameter, this corresponds to 150,000 electrons being modulated into, and out of the monolayer.

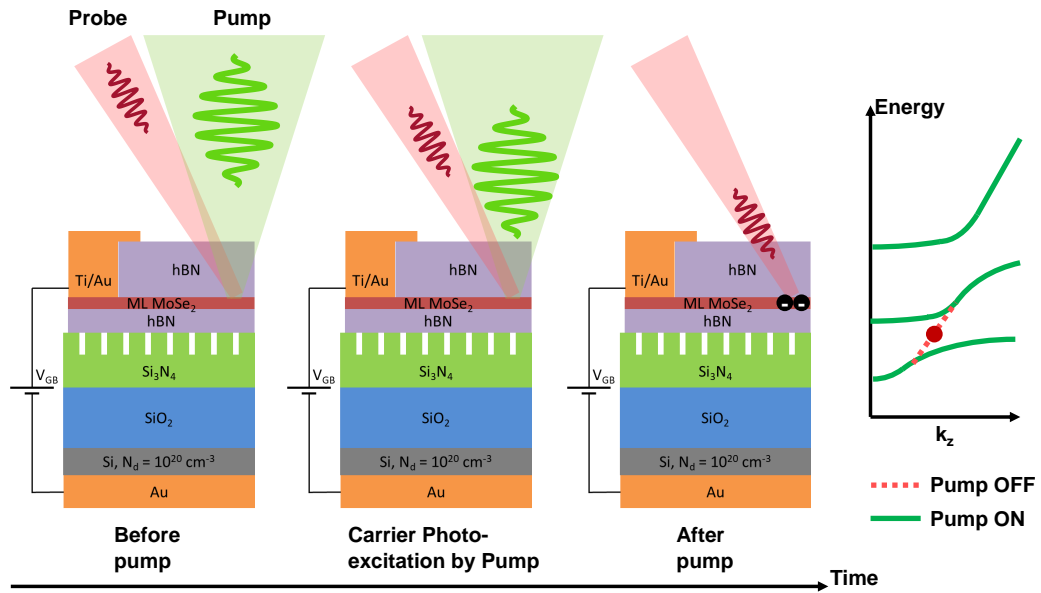


Figure 5.1: All-optical low-power modulators based on exciton-trion-polaritons. A pump pulse arrives on the sample; photoexcites new carrier pairs, some of which result in a transient net background carrier density. The optical response of polaritons is thus modified when the probe arrives. If the probe pulse is tuned to a part of the polariton dispersion, turning on or off the pump pulse results in modulation of the probe. Efficiency of such a scheme is discussed in the main text.

If background electrons in the TMD device is photo-generated, all-optical modulators such as the one shown in 5.1 could be realized. Ultrafast spec-

troscopy measurements of TMDs, show that large carrier density modulations are possible with optical pump pulses. A majority of these transient carriers rapidly recombine within picoseconds [72], which allows for ultrafast all-optical modulators. A practical estimation using experimental data based on Chapter 4 shows that, when assuming that 1% of the photoexcited carriers are converted to electrons [62], less than 600 fJ/pulse is needed for a probe modulation depth of 10%. In order to push these devices into the single-photon regime, the monolayer of MoSe₂ could be replaced with heterobilayers of TMDs. Interlayer excitons [40] and trions [4, 17] have been shown to exist in these systems. High efficiencies involved in charge transfer processes that capture free photo-excited electron-hole pairs [40].

Another interesting application comes from applying lateral electric fields to exciton-trion-polaritons. While recent investigations [8] focused on accelerating charged-polaritons with electric fields, results in this area go back to III-V research [65]; III-V systems have shown drift of exciton-trion states under electric fields, as well as charged-exciton-polariton beam steering [8]. As III-V trion binding energies are ~ 3 meV, only small electric fields could be used to accelerate trions in these systems without ionizing them. Instead, TMD systems have binding energies 10 times larger (see Chapter 2), and the lower mobility of TMD systems could be recovered by hBN-encapsulated devices [73].

5.1.2 Exciton-Trion-Polariton Metasurfaces

Exciton-trion-polariton systems based on ultrafast carrier density modulation is promising; but by no means optimal. While the optical conductivity changes

due to Coulomb-coupling of exciton-trion states is very large, the effect of this conductivity change to the overall optical device modulation is restricted by the optical mode overlap with the TMD monolayer. Compared to a micron-sized mode profile possessed by the optical mode, the exciton-trion superposition states are localized to less than a nm size [20]. Fabrication of DBR cavities [64], or 2D photonic crystals somewhat localize photons to the vicinity of the monolayer. To continue along this trend, metasurfaces could be employed to optimize mode overlap further than can be achieved by simple periodic photonic crystals.

Fig 5.2b shows an example of how such a metasurface could be fabricated. In essence, the device would be a one-dimensional photonic crystal cavity. However, the part of the top mirror could be patterned into a metasurface. Thus, such a structure would obtain a trade-off between vertical and horizontal mode confinement. If further mode confinement is needed, the device could be etched vertically to provide additional mode overlap. For a device that is normally n-doped, the metasurface could be optimized for a TMD with optical conductivity shown in the blue curve of Fig 5.2a. Then, an optical pulse can generate photo-excited electron-hole pairs, some of which recombine and leave a net electron density. This transient electron doping would largely affect the optical conductivity. Since the metasurface was optimized for the low-doping state, the optical response of the metasurface around the ET resonance area would be dramatically, and rapidly altered. Then, this system becomes an all-optical transistor. The configuration described above is equivalent to the "normally-on" configuration of transistors. If the transient carrier density is known, the device could be designed for the optical conductivity reached by the monolayer after the pulse. Such a configuration would be "normally-off."

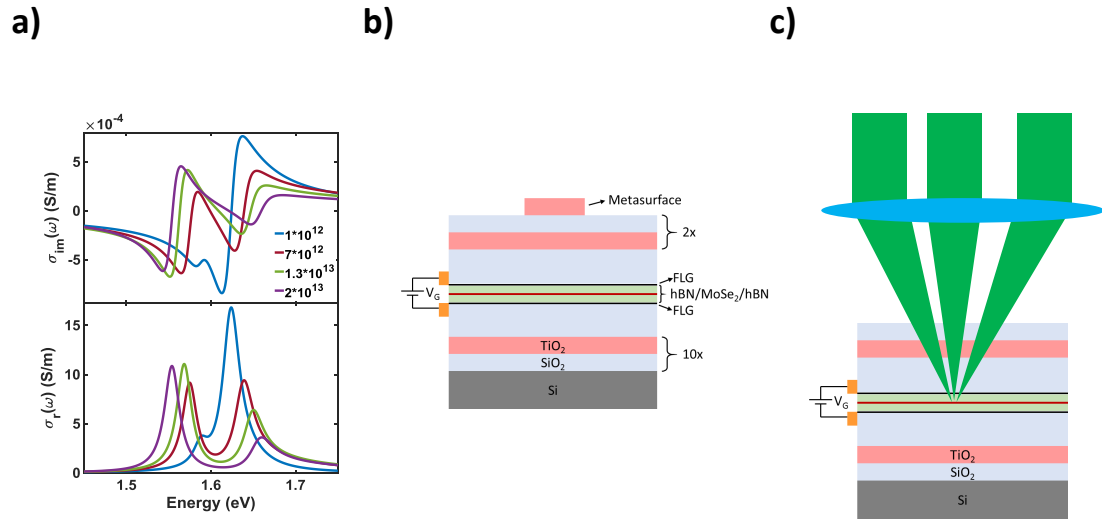


Figure 5.2: Concept of exciton-trion-polariton metasurfaces. a. Change of real and imaginary optical conductivity with background carrier density. To translate these large optical conductivity changes to large optical response modulation, metasurfaces that optimize mode profile must be engineered. b. A proposed metasurface structure, where the top mirror was “weakened” to pattern the metasurface. How this device could operate as “normally on” or “normally off” all-optical transistors is qualitatively described in the main text. c. Transient metasurfaces by spatial and temporal light modulation. The incoming beam could be shaped to allow a particular pump pulse shape on the sample. This shape will then cause a transient carrier density modulation over the sample, which could then affect optical response of the system to a probe pulse.

Instead of shaping the photonic crystals to be the metasurface, optical pulses could be shaped in time and space to serve as a transient metasurface, as depicted in Fig 5.2c. While mode overlap would not be optimized in this case, a rapidly reconfigurable transient metasurface could be useful in classical photonics applications.

Of course, all of the applications above assume exciton-trion-polariton devices where pump and probe are incoherent. It is fair to anticipate coherent spectroscopy of exciton-trion-polaritons to yield many other device applications

that are further optimized for performance.

5.2 Conclusion

Either from a fundamental science point of view, or concerning its device applications, exciton-trion-polaritons hide a veritable treasure-trove of new discoveries waiting to be made. Remarkable agreement between theoretical predictions by Rana et al. [58, 22], and the experiments discussed in Chapters 2-3 implies that the trion-photon interaction has now a strong theoretical basis. Chapter 4 demonstrated the first forays into controlling such a system. The promise of such a strongly-coupled system is hard to overstate: a two-dimensional electron gas that possesses strong Coulomb-coupled correlated states, spin-valley polarization, and efficient creation of the correlated states by photons and vice versa is guaranteed to lead to plenty exciting new scientific discoveries, and to numerous device applications.

APPENDIX A

CRYOGENIC CONFOCAL MICROSCOPE ALIGNMENT DETAILS

All of the alignment protocols described in the main text conjugate either the sample image plane or the objective back-focal plane with the spectrometer (monochromator) entrance slit; the sample image plane for spatially-resolved, and the back-focal plane for energy-momentum spectroscopy measurements. However, in order to obtain the best quality of spectroscopic data, the monochromator slit must be imaged with minimal aberrations onto the Charge-Coupled Device (CCD) camera used in measurements. If this step is done carelessly, defocusing, astigmatism, or coma artifacts would dominate the qualitative features of the measurement; making it extremely difficult to obtain accurate spectroscopic information from which to extract important physical details about the sample.

A.1 Aligning the Monochromator and CCD

Assuming that the microscopy setup is being built from scratch, the first step one needs to take is to define a precise optical axis to which the monochromator will be aligned. This is typically done iteratively using two irises. These irises are affixed to the machined holes on the optical table, ideally more than a meter apart. By passing a single laser beam through the center of both irises, which should be at the same height from the table, an optical axis whose precision matches the machining accuracy with which the optical table platform was built can be obtained.

Once this step is complete, the monochromator is placed such that its en-

trance slit, closed to about 200 microns, and its center aperture are co-axial with optical axis defined by the laser. To obtain the unique monochromator alignment, the center of the first convex lens of the monochromator has to be co-axial with the laser, also. Input slit and convex lens alignments have to be iteratively corrected until both are co-axial with the laser beam-defined axis. Now, the monochromator's internal alignment should ensure that the laser beam travel all the way from the front slit to the back slit. To confirm this is indeed the case, one can use the 0th-order diffraction of the grating being used in measurements. This should reflect the beam along the optical axis of the monochromator, and send it out through the front exit slit. Roughly 1/3rd of light should come through, due to the quantum efficiencies of the spectrometer parts. If the spectrometer is being aligned from scratch, it is important to confirm that the 0-th order diffraction position of the monochromator (shown as the 0nm wavelength) should be exactly where this 1/3rd response is. If not, the position where maximum laser transmission is found should be redefined as the new calibration zero of the monochromator.

Once this stringent alignment is complete, the side mirror should be engaged. The path defined by this side mirror is where the CCD will be aligned. Here, two methods could be utilized to obtain high-quality alignment between the monochromator input slit and the CCD image plane. A spectral calibration lamp could either be placed immediately before a nearly-closed front input slit, or at the image plane of the entire setup. The spectral lines of the lamp are extremely narrow, and should serve as "Dirac-delta" spectral responses with which to calibrate lamp alignment. One of the bright spectral lines of the calibration lamp near the wavelengths that will be used in experiments should be selected as the monochromator target wavelength. Now, the camera should be

brought into alignment while continuous spectra are taken every 250 milliseconds. The angle and focal depth of the camera can easily be changed using the CCD flange. Meanwhile, a slight tilt of the monochromator can be used to correct for spectral aberrations of the dispersion image. Once the calibration lamp image is as narrow as 1-2 pixels, the calibration is complete. However, for E-k dispersion, off axis resolution is equally important. To ensure this is up to par, a spectrum image should be taken. Care should be taken that the spectral response of the camera looks like a narrow line across the vertical axis. In this image mode calibration, light must be allowed to pass through the entire height of the front input slit.

It is useful to note that the diffraction grating disperses photons by wavelength along only the horizontal direction. This will become useful in the section where vertical pixels will be mapped to photon momentum.

A.2 Mapping Horizontal Pixels to Wavelength

During the previous calibration above, if everything was done ideally, the target spectral emission line that the monochromator was calibrated to should have fallen on the center pixel of the CCD. Say, for a 1024 pixel CCD, this would mean that the 512th pixel should show the spectral line. However, when the monochromator target wavelength is changed, the same emission no longer falls on the 512th pixel. So, a map between pixel index to photon number must be developed. This map is achieved with the following MATLAB script:

```

%wave length at the center of array in nm
CWL = 775;
%order of diffraction (1,2,3.....)
DO = 1;
%groves/mm
GD = 600;

pixel_center = 512;
pixel_start = 1;
pixel_end = 1024;

% Monochromator Info
pixel_size = 0.026; %[mm]
% pixel array
pixel = pixel_start:1:pixel_end;
% output focal length iHR320 in mm
focal_length = 319.719;
% Inclination of the focal plane measured
% at the location normally occupied by the exit slit
focal_plane_angle = 0.5;
% included angle (degrees)
% Equals input Ebert angle + output Ebert angle.
Dv = 21.26;

% Step 1. Find out Angle Beta at the center of CCD

```

```

% input angle in degree
alpha_center = asin(1e-6*DO*GD*CWL/(2*cos(Dv/2*pi/180)))/pi*180-Dv/2;
% output angle in degree
beta_center = Dv+alpha_center;

% Step 2. Find out lamda
% Perpendicular distance from grating
% or focusing mirror to the focal plane (mm)
LH      = focal_length*cos(pi*focal_plane_angle/180);
% Distance from the intercept of the
% normal to the focal plane to the wavelength
HBC     = focal_length*sin(pi*focal_plane_angle/180);
BH      = beta_center+focal_plane_angle;
HBn     = pixel_size.*(pixel-pixel_center) + HBC;
Beta_n  = BH-atan(HBn./LH)./pi.*180;

lamda   = (sin(alpha_center*pi/180)+sin(Beta_n*pi/180)).*1e6./DO./GD;

```

A.3 Mapping Vertical Pixels to Photon Momentum

For E-k dispersion measurements, vertical pixels have to be mapped to the photon momentum besides the horizontal pixels being mapped to photon energy. This step needs to be completed once the photon energy is calculated, as the momentum of a photon incident on the CCD pixel depends on the energy that photon carries. Once the energy and momentum are mapped, the processed

data becomes a projective transform of the initial pixel array data. Correctly plotting such a data structure requires a pseudocolor plot where x and y coordinates of each data point are mapped. Also, during E-k map measurements, the resolution limit of the CCD is 4-8 pixels. Thus, information on one pixel and on pixels in its immediate vicinity are redundant. This redundancy could be leveraged, without loss of information being carried by photons into the CCD, by Gaussian smoothing the data. This was achieved by interpolating the data four-fold, and running a Gaussian smoothing kernel of 16 pixel radius on the data. The MATLAB script used to achieve all of this is attached below:

```
% Interpolating Image to Reduce Coarseness
htmDisp = getimage();
%
dE = (E(2)-E(1))./4;
dx = .25;

x2 = x(1):dx:x(end); % Interpolated array for x
%Ep = E+dE;

E2 = [];

% Only works if array spacing is bigger than dE
for i = 1:length(E)
E2 = [E2 E(i) E(i)+dE E(i)+2*dE E(i)+3*dE];
end

[xm, Em] = meshgrid(x,E);
```

```

[xm2, Em2] = meshgrid(x2,E2);

Disp2 = interp2(xm,Em,htmDisp,xm2,Em2);

%% Mapping k vectors to pixel array

Temp = Disp2(:,16:end);

Temp2 = imgaussfilt(Temp,16);
RSdisp = zeros(size(Temp2));

hbarC = 0.197326980; % hbar*c product [eV*um]

NA = 0.6;
pixel_0 = 135; % Pixel where mode is centered
pixel_end = 1; % Pixel where objective NA is reached

th_max = asin(NA); % Maximum angle collected by objective
th_x = atan(tan(th_max)*(x2(16:end)-pixel_0)./(pixel_end-pixel_0));
% Angle(pixel) [rad]
k0 = E2./hbarC;
k_z_th_grid = k0.'*sin(th_x);
k = k_z_th_grid(length(E2),:);

for i = 1:length(E2)-1
RSdisp(length(E2)-i,:) = interp1(k_z_th_grid(length(E2)-i,:))...

```

```

...,Temp2(length(E2)-i,:),k_z_th_grid(length(E2),:),'linear',0);
% Rescale each horizontal array of pixels with the
%correct scale of k vectors, extrapolate values to 0
end
%
figure;
sss = pcolor(k, E2, RSdisp);
set(gca, 'ydir','normal');
set(gca, 'xdir','normal');

```

A.4 Liquid Helium Transfer Procedure

Preparations for helium-based measurements start a few days in advance of the actual process. If the helium transfer line has not been evacuated for more than 3 months, a one-week pump-down of the transfer line is undertaken. During this week, the entire measurement setup is aligned and tested with the sample mounted in the cryostat and placed in vacuum. After the dry run is completed, the sample is left attached to the vacuum pump overnight. This ensures that a high vacuum is held for at least an 8-12 hour period following the pump's disconnection. This 12-hour window is where the measurements will take place. The first thing done in the experiment day is the liquid helium transfer. The following procedure summarizes the best practices accumulated by the author:

1. Ensure enough vertical clearing is present to place bottom of the transfer line directly over the helium Dewar transfer line insert.

2. Close the 2-psi release valve, and open the vent valve.
3. Leave the VC30 open knob only about half a turn from fully closed. Leave the transfer line flow knob open about $1/8^{th}$ of a turn.
4. Slowly and continuously insert the tube until 13 inches remain. This is the point where the transfer line will contact the liquid helium and begin boiling it off.
5. Slow down insertion rate once a white plume, which is pressurized helium gas, begins to vent through the open valve.
6. Once the tube is about 3-4 inches over the bottom of the Dewar, rapidly lower the tube all the way to the bottom. This will boil enough helium to build up pressure to force liquid helium to flow into the cryostat in subsequent steps.
7. Quickly screw cap residing on the transfer line into the Dewar top insert cover threads to prevent helium from escaping; building up pressure.
8. Quickly close vent valve, and turn on the VC30 pump. This pump controls the exhaust rate of the liquid helium. If done correctly, the helium should flow within 5 minutes. If no flow occurs, remove the transfer line, heat it, and remove any moisture before trying again.

Liquid helium flow can be confirmed when the negative pressure pump sounds different due to helium going through it. Also, the negative pressure built up in the VC30 will somewhat release after flow begins. Afterwards, fully close the transfer line flow knob, and open it $1/32 - 1/16^{th}$ of a turn. Then, lower the VC30 flow knob until the gauge reads almost no helium flow. If temperature stops dropping, that means flow was stopped. Opening either the VC30 or the

transfer line knob should bring back flow. Otherwise, the best practice is to lower the flow to about 0.3 degrees per second.

This step of lowering flow rate until the bare minimum not only conserves helium, but it also allows a thermo-mechanical breathing mode from occurring. If not prevented, this thermo-mechanical noise will move the sample up and down by about $10\ \mu\text{m}$ or more. It is predicted that only cold helium gas makes contact to copper when flow rate is lowered, so the heat capacity of the cooling medium does not suffer any sudden changes as would be the case with a helium gas-liquid mixture. With the near-constant heat capacity, the heater built into the cryostat can easily control the temperature variation to below 10 mK.

Of course, using varying laser or white light powers will change the device temperature. It is also a guarantee that the sample will be much hotter than the thermocouple readout. In the case of our exciton-trion-polariton experiments, these issues were not detrimental, as the spectral feature of trions were found to be robust up to 100 K. Optical pump powers exceeding this thermal budget are so large that the monolayer MoSe_2 would be optically damaged before the system temperature reached 100 K.

APPENDIX B

FINITE-DIFFERENCE FREQUENCY-DOMAIN MEASUREMENTS

Theoretical fits of the measured dispersion data in Chapter 3 were realized using the Finite-Difference, Frequency-Domain measurements technique [79] by Minwoo Jung. Reflectivity measurements using FDFD were done by having a plane wave with frequency ω and wave vector (\vec{k} was excited at a planar port located well above a unit cell of the structure being simulated, and the reflection coefficient was extracted as the scattering matrix element evaluated at the same port. Dispersion was obtained by measuring different (\vec{k}, ω) pairs. For each measurement, a single unit cell of the photonic crystal was used with periodic boundary conditions. These measurements were normalized by the reflectivity spectrum of the unpatterned $\text{Si}_3\text{N}_4/\text{SiO}_2/\text{Si}$ thin film.

Consistent with optical metrology measurements, refractive indexes of SiO_2 , Si_3N_4 , and Si were taken as 1.46, 2.00, and 3.7, respectively. To account for slight fabrication inaccuracies, normalized reflectivity of the grating structure without the monolayer was measured. The best fits to experimental data were used to determine the thickness of the grating.

As previously mentioned, the contribution to the photon self-energy $\Sigma^{ph}(\vec{k}, \omega)$ from excitons/trions can be expressed in terms of the 2D optical conductivity $\sigma(\vec{k}, \omega)$ of the MoSe_2 ML,

$$\Sigma^{ph}(\vec{k}, \omega) = -i\hbar \frac{|\chi(z^*)|^2}{2\langle\epsilon\rangle} \sigma(\vec{k}, \omega) \quad (\text{B.1})$$

where, $\chi(z^*)$ is the waveguide mode amplitude at the location z^* of the ML and $\langle\epsilon\rangle$ is the average dielectric constant experienced by the waveguide mode. Therefore, the MoSe_2 ML in FDFD simulations was modeled as a layer of

thickness $d = 0.7$ nm [20] with a 3D optical conductivity $\sigma_{total}(\vec{k}, \omega)$ given by, $\sigma_{total}(\vec{k}, \omega) = \sigma(\vec{k}, \omega)/d - i\epsilon\omega$. Here, $\epsilon = 20\epsilon_0$ is the high-frequency dielectric constant of MoSe₂ resulting from optical transitions at energies higher than the exciton-trion energies [78]. The expression for the 2D optical conductivity $\sigma(\vec{k}, \omega)$ of the MoSe₂ ML is given by Rana et al. [22]. Parameters of this model are the exciton and trion lifetimes, and the optical bandgap.

By placing this 3D conductor over the photonic crystal grating structure whose dimensions were determined by the best-fit estimated as outlined above, the exciton-trion-polariton dispersion was measured. Since exciton and trion lifetimes were determined by photoluminescence measurements in the weak coupling limit, only the optical bandgap was used as a free parameter to obtain the precise agreement between data and theory seen in Chapter 3.

APPENDIX C

**POTENTIAL METHODS TO IMPROVE EXCITON-TRION-POLARITON
DEVICE QUALITY**

C.1 Disorder in 2D Layered Materials

A great deal of improvement for exciton-trion-polariton devices is based on improvements done on the two-dimensional material quality. In a recent review [15], disorder in two-dimensional materials was broadly categorized into two separate camps; extrinsic and intrinsic.

To mitigate intrinsic disorder, which encompasses vacancy, anti-site, and substitutional defects [15], the best course of action is to improve the quality of bulk grown two-dimensional materials. Promising improvements in bulk two-dimensional material growth, through techniques such as flux-zone growth [14, 15], intrinsic disorder was mitigated to a significant extent. Further improvements against substitutional oxygen defects [63] could be done by engineering dry-transfer steps to be done in nitrogen glove boxes, or under vacuum.

As such, recent measurements on flakes of graphene and MoS₂ directly exfoliated onto thin film substrates, not unlike the polymer-transferred monolayer MoSe₂ flake in the exciton-trion-polariton device of Chapter 3, showed extrinsic disorder to be the primary reason for degradation of device quality [15]. Strain, surface roughness or dangling bonds, and adsorbates all locally affect the local electric potential of the monolayer, causing charge "puddles" to form. Recent scanning-tunneling microscopy techniques have confirmed the presence of such charge disorder in monolayer TMDs exfoliated directly onto thin-film

substrates [15]. Further perturbations due to strain even include local changes to band structure. Such perturbations would induce a trapping potential localizing excitons. Meanwhile, extrinsic impurities have been shown to cause broadening of excitonic resonances in TMDs [19].

C.2 Contamination-Free Dry Transfer Using Polymer-Based Stamps

Part of these problems are mitigated simply by screening the local dielectric environment by introducing a high-quality dielectric, such as hBN, in between the monolayer TMD and the thin film substrates. Such an attempt has been made in the device discussed in Chapter 4. While the introduction of hBN greatly reduces disorder caused by the thin film substrate, it still leaves behind local strain, and adsorbates due to residues between the TMD and hBN layer.

In the device discussed in Chapter 4, dry-transfer was achieved by sequential PDMS transfer steps, each of which followed the procedure outlined in Chapter 2. In each of these steps, the "top" surface of the TMD or hBN layer was in direct contact with PDMS. It has been shown that [1] dimethoxysilane functional groups remain in the interface between bottom hBN and TMD monolayer. While Jain et al chose to use UV-ozone cured PDMS [1] to form these chemical groups into a thin, inert silica layer, the fabrication process outlined in Chapter 4 avoided this due to the brittleness of the UV-cured polymers failing to adhere onto the grating structures, which have air gaps dramatically reducing adhesion.

A much better method relies on the electrostatic attraction between hBN and TMDs [21]. In this method, a polymer is used to pick up an hBN flake, which in turn is used to pick up a monolayer. The resulting stack is brought in alignment with a bottom hBN flake, and a complete stack is made. In preparing these flakes, it is important to ensure that each flake was exfoliated from bulk, instead of being dry-transferred directly from tape. Otherwise, tape residue will be present on the top surfaces of each tape-transferred flake; dramatically reducing device quality.

By carefully engineering the shape of the dry-transfer stamps into spherical shapes, strain in each 2D material interface could be significantly removed. While strides were made in pursuit of this Thesis in design of such stamps, these dry-transfer stamps were not included in fabrication of any of the devices discussed in the Thesis.

APPENDIX D
RECENT RESULTS SIMILAR TO THAT OF
EXCITON-TRION-POLARITONS

During the time experiments described in this Thesis was undertaken, similar experimental demonstrations were published by two groups in journals, while a third demonstration similar to the work in Chapter 4 was published in a conference proceedings. Similarity between the theory described in Chapter 1 to Fermi-Polaron-Polaritons [46] has already been discussed. In a similar vein, qualitative demonstrations of electrostatic control of exciton-trion-polariton dispersion discussed in Chapter 4 corroborates results by Imamoglu et al. [46]. However, a similar experiment done by Vamivakas et al., [64] where a monolayer of MoSe₂ was placed at the mode maximum of a high Q-factor DBR cavity showed a LP band with negative effective mass, which cannot be explained by the model described in Chapter 1. While the design of devices for the results in Chapter 4 was underway, a conference proceeding published by Kondratyev et al. demonstrated electrostatic control of what resembles exciton-trion-polaritons [34]. One interesting aspect of this device is that the diffraction grating is fabricated by Ta₂O₅, which has been shown to have exceptionally high dielectric constants in DC frequencies [42]. Modulation of this layer to obtain a grating should cause significant modulation of the carrier density across a single unit cell. Effects of such a carrier density modulation is not understood, and could be a subject of further investigation.

BIBLIOGRAPHY

- [1] A. Jain, P. Bharadwaj, S. Heeg, M. Parzefall, T. Taniguchi, K. Watanabe, L. Novotny. Minimizing residues and strain in 2d materials transferred from pdms. *Nanotechnology*, 29:265203, 2018.
- [2] Alexey Chernikov, Arend M. van der Zande, Heather M. Hill, Albert F. Rigosi, Ajanth Velauthapillai, James Hone, Tony F. Heinz. Electrical tuning of exciton binding energies in monolayer ws_2 . *Phys. Rev. Lett.*, 115:126802, 2015.
- [3] B. K. Choi, M. Kim, K.-H. Jung, J. Kim, K.-S. Yu, Y. J. Chang. Temperature dependence of band gap in MoSe_2 grown by molecular beam epitaxy. *Nanoscale Res. Lett.*, 12:492, 2017.
- [4] Mauro Brotons-Gisbert, Hyeonjun Baek, Aidan Campbell, Kenji Watanabe, Takashi Taniguchi, and Brian D. Gerardot. Moiré-trapped interlayer trions in a charge-tunable $\text{wse}_2/\text{mose}_2$ heterobilayer, 2021.
- [5] Tim Byrnes, Na Young Kim, and Yoshihisa Yamamoto. Exciton-polariton condensates. *Nat. Physics*, 10(11):803–813, 2014.
- [6] C. Lee, H. Yan, L. E. Brus, T. F. Heinz, J. Hone, S. Ryu. Anomalous lattice vibrations of single- and few-layer MoS_2 . *ACS Nano*, 5:2695, 2010.
- [7] C. Tonndorf, R. Schmidt, P. Böttger, X. Zhang, J. Börger, A. Liebig, M. Albrecht, C. Kloc, O. Gordan, D. R. T. Zahn, S. Michaelis de Vasconcellos, R. Brachstich. Photoluminescence emission and raman response of monolayer mos_2 , mose_2 , and wse_2 . *Opt. Express*, 4:4908, 2013.
- [8] T. Chervy, P. Knüppel, H. Abbaspour, M. Lupatini, S. Fält, W. Wegscheider, M. Kroner, and Atac Imamoglu. Accelerating polaritons with external electric and magnetic fields. *Phys. Rev. X*, 10:011040, 2020.
- [9] S. Christopoulos, G. Baldassarri Höger von Högersthal, A. J. D. Grundy, P. G. Lagoudakis, A. V. Kavokin, J. J. Baumberg, G. Christmann, R. Butté, E. Feltn, J.-F. Carlin, and N. Grandjean. Room-temperature polariton lasing in semiconductor microcavities. *Phys. Rev. Lett.*, 98:126405, 2007.
- [10] M. Combescot and O. Betbeder-Matibet. The trion as an exciton interacting with a carrier. *Solid State Commun.*, 126(12):687 – 691, 2003.

- [11] Combescot, M. and Tribollet, J. Trion oscillator strength. *Solid State Commun.*, 128:273–277, 2003.
- [12] Jorge Cuadra, Denis G. Baranov, Martin Wersäll, Ruggero Verre, Tomasz J. Antosiewicz, and Timur Shegai. Observation of tunable charged exciton polaritons in hybrid monolayer ws_2 plasmonic nanoantenna system. *Nano Lett.*, 18(3):1777–1785, 2018.
- [13] D. K. Efimkin, A. H. MacDonald. Many-body theory of trion absorption features in two-dimensional semiconductors. *Phys. Rev. B*, 95:035417, 2017.
- [14] D. Rhodes, R. Schönemann, N. Aryal, Q. Zhou, Q. R. Zhang, E. Kampert, Y.-C. Chiu, Y. Lai, Y. Shimura, G. T. McCandless, J. Y. Chan, J. Y. Chan, D. W. Paley, J. Lee, A. D. Finke, J. P. C. Puff, S. Das, E. Manousakis, L. Balicas. Bulk Fermi surface of the Weyl type-II semimetallic candidate $\gamma\text{-MoTe}_2$. *Phys. Rev. B*, 96:165134, 2017.
- [15] D. Rhodes, S. H. Chae, R. Ribiera-Palau, J. Hone. Disorder in van der waals heterostructures of 2D materials. *Nat. Mater.*, 18:541, 2019.
- [16] B. E. Deal and M. Sklar. Thermal oxidation of heavily doped silicon. *The Electrochemical Society*, 112(4):430, 1965.
- [17] Thorsten Deilmann and Kristian Sommer Thygesen. Interlayer trions in the mos_2/ws_2 van der waals heterostructure. *Nano Letters*, 18(2):1460–1465, 2018. PMID: 29377700.
- [18] Hui Deng, Hartmut Haug, and Yoshihisa Yamamoto. Exciton-polariton bose-einstein condensation. *Rev. Mod. Phys.*, 82:1489–1537, 2010.
- [19] Magdulin Dwedari, Samuel Brem, Maja Feierabend, and Ermin Malic. Disorder-induced broadening of excitonic resonances in transition metal dichalcogenides. *Phys. Rev. Materials*, 3:074004, Jul 2019.
- [20] F. Cadiz, C. Robert, G. Wang, W. Kong, X. Fan, M. Blei, D. Lagarde, M. Gay, T. Taniguchi, K. Watanabe, T. Amand, X. Marie, P. Renucci, S. Tongay, B. Urbaszek. Ultra-low power threshold for laser induced changes in optical properties of 2D molybdenum dichalcogenides. *2D Mater.*, 3:045008, 2016.
- [21] F. Pizzocchero, L. Gammelgaard, B. S. Jessen, J. M. Cariad, L. Wang, J. Hone, P. Bøggild, and T. J. Booth. The hot pick-up technique for batch assembly of of van der Waals heterostructures. *Nat. Commun.*, 7:11894, 2016.

- [22] Farhan Rana, Okan Koksal, Christina Manolatou. Many-body theory of the optical conductivity of excitons and trions in two-dimensional materials. *Phys. Rev. B*, 102:085304, 2020.
- [23] Gabriella D. Shepard, Jenny V. Ardelean, Obafunso A. Ajayi, Daniel Rhodes, Xiaoyang Zhu, James C. Hone, Stefan Strauf. Trion-species-resolved quantum beats in mose_2 . *ACS Nano*, 11:11550–11558, 2017.
- [24] H. Nan, Z. Wang, W. Wang, Z. Liang, Y. Lu, Q. Chen, D. He, P. Tan, F. Miao, X. Wang, J. Wang, Z. Ni. Strong photoluminescence enhancement of MoS_2 through defect engineering and oxygen bonding. *ACS Nano*, 8:5738, 2018.
- [25] H. Wang, C. Zhang, F. Rana. Ultrafast dynamics of electron-hole recombination in monolayer MoS_2 . *Nano Lett.*, 15:339, 2014.
- [26] Paul Harrison. *Excitons*, chapter 6, pages 189–218. John Wiley & Sons, Ltd, 2005.
- [27] Hartmut Haug and Stephan W. Koch. *Quantum theory of the optical and electronic properties of semiconductors, fifth edition*. World Scientific Publishing Co., January 2009. Publisher Copyright: © 2009 by World Scientific Publishing Co. Pte. Ltd. All rights reserved. Copyright: Copyright 2017 Elsevier B.V., All rights reserved.
- [28] K. Hennessy, A. Badolato, M. Winger, D. Gerace, M. Atatüre, S. Gulde, S. Fält, E. L. Hu, and A. Imamoglu. Quantum nature of a strongly coupled single quantum dot-cavity system. *Nature*, 445(7130):896–899, 2007.
- [29] K. Wang, K. D. Greve, L. A. Jauregui, A. Sushko, A. High, Y. Zhou, G. Scuri, T. Taniguchi, K. Watanabe, M. D. Lukin, H. Park, P. Kim. Electrical control of charged carriers and excitons in atomically thin materials. *Nat. Nano*, 13:128–132, 2018.
- [30] K. Kheng, R. T. Cox, Merle Y. d’ Aubigné, Franck Bassani, K. Saminadayar, and S. Tatarenko. Observation of negatively charged excitons x^- in semiconductor quantum wells. *Phys. Rev. Lett.*, 71:1752–1755, Sep 1993.
- [31] Kin Fai Mak, Keliang He, Changgu Lee, Gwan Hyoung Lee, James Hone, Tony F. Heinz, Jie Shan. Tightly bound trions in monolayer mos_2 . *Nat. Mater.*, 12:207, 2012.

- [32] Mackillo Kira and Stephan W. Koch. *Semiconductor Quantum Optics*. Cambridge University Press, 2011.
- [33] Patrick Knüppel, Sylvain Ravets, Martin Kroner, Stefan Fält, Werner Wegscheider, and Atac Imamoglu. Nonlinear optics in the fractional quantum hall regime. *Nature*, 572(7767):91–94, 2019.
- [34] V. Kondratyev, F. Benimetskiy, T. Ivanova, A. Samusev, K.-D. Park, D. N. Krizhanovskii, M. S. Skolnick, E. Khestanova, V. Kravtsov, and I. Iorsh. Electrically tunable trion-polaritons in mose2/hbn heterostructure integrated with a photonic crystal slab. *AIP Conference Proceedings*, 2300(1):020062, 2020.
- [35] K. Koshelev, M. A. Mohammad, T. Fito, K. L. Westra, S. K. Dew, and M. Stepanova. Comparison between zep and pmma resists for nanoscale electron beam lithography experimentally and by numerical modeling. *J. Vac. Sci. Technol. B*, 29:06F306, 2011.
- [36] L. Xie, L. Du, X. Lu, R. Yang, D. Shi, and G. Zhang. A facile and efficient dry transfer technique for two-dimensional van der Waals heterostructure. *Chin. Phys. B*, 26:087306, 2017.
- [37] Konstantinos Lagoudakis. December 2013.
- [38] Murray A. Lampert. Mobile and immobile effective-mass particle complexes in nonmetallic solids. *Phys. Rev. Lett.*, 1:12, 1958.
- [39] S.-Y. Lee, T.-Y. Jeong, S. Jung, and K.-J. Yee. Refractive index dispersion of hexagonal boron nitride in the visible and near-infrared. *Phys. Status Solidi B*, 256:1800417, 2019.
- [40] Zidong Li, Xiaobo Lu, Darwin F. Cordovilla Leon, Zhengyang Lyu, Hongchao Xie, Jize Hou, Yanzhao Lu, Xiaoyu Guo, Austin Kaczmarek, Takashi Taniguchi, Kenji Watanabe, Liuyan Zhao, Li Yang, and Parag B. Deotare. Interlayer exciton transport in mose2/wse2 heterostructures. *ACS Nano*, 15(1):1539–1547, 2021.
- [41] D. G. Lidzey, D. D. C. Bradley, M. S. Skolnick, T. Virgili, S. Walker, and D. M. Whittaker. Strong exciton-photon coupling in an organic semiconductor microcavity. *Nature*, 395(6697):53–55, 1998.
- [42] Jun Lin, Nakabayasi Masaaki, Atsuhiko Tsukune, and Masao Yamada.

Ta₂O₅ thin films with exceptionally high dielectric constant. *Applied Physics Letters*, 74(16):2370–2372, 1999.

- [43] Long Zhang, Rahul Gogna, Will Burg, Emanuel Tutuc, Hui Deng. Photonic-crystal exciton-polaritons in monolayer semiconductors. *Nat. Commun*, 9:713, 2018.
- [44] M. Combescot, O. Betbeder-Matibet, F. Dubin. The trion: Two electrons plus one hole versus one electron plus one exciton. *Eur. Phys. J. B*, 42:63–83, 2004.
- [45] M. R. Molas, C. Fagueras, A. O. Slobodeniuk, K. Nogajewski, M. Bartos, D. M. Basko, M. Potemski. Brightening of dark excitons in monolayers of semiconducting transition metal dichalcogenides. *2D Mater.*, 4:021003, 2017.
- [46] Meinrad Sidler, Patrick Back, Ovidiu Cotlet, Ajit Sristava, Thomas Fink, Martin Kroner, Eugene Demler, Atac Imamoglu. Fermi polaron-polaritons in charge-tunable atomically thin semiconductors. *Nat. Phys*, 13:255–261, 2016.
- [47] Shiue-Yuan Shiao Monique Combescot. *Excitons and Cooper Pairs: Two Composite Bosons in Many-Body Physics*. Oxford Graduate Texts, 2015.
- [48] N. Lundt, E. Cherotchenko, O. Iff, Fan Y. Shen, P. Bigenwald, A. V. Kavokin, S. Höfling, C. Schneider. The interplay between excitons and trions in a monolayer of mose₂. *Appl. Phys. Lett.*, 112:031117, 2018.
- [49] Gal Ness, Constantine Shkedorov, Yanay Florshaim, Oriana K. Diessel, Jonas von Milczewski, Richard Schmidt, and Yoav Sagi. Observation of a smooth polaron-molecule transition in a degenerate fermi gas. *Phys. Rev. X*, 10:041019, Oct 2020.
- [50] O. A. Ajayi, J. V. Ardelan, G. D. Shepard, J. Wang, A. Anthony, T. Taniguchi, K. Watanabe, T. F. Heinz, S. Strauf, X Zhu, J. C. Hone. Approaching the intrinsic photoluminescence linewidth in transition metal dichalcogenide monolayers. *2D Mater*, 4:031011, 2017.
- [51] Seoung-Hwan Park, Doyeol Ahn, Yong-Tak Lee, and Shun-Lien Chuang. Exciton binding energies in zincblende GaN/AlGaN quantum wells. *Japanese Journal of Applied Physics*, 43(1):140–143, jan 2004.

- [52] Stanley Pau, Gunnar Björk, Joseph Jacobson, Hui Cao, and Yoshihisa Yamamoto. Microcavity exciton-polariton splitting in the linear regime. *Phys. Rev. B*, 51:14437–14447, 1995.
- [53] Q. Cao, F. Grote, M. Hußmann, S. Eigler. Emerging field of few-layered intercalated 2d materials. *Nanoscale Adv.*, 3:963, 2021.
- [54] Y. Rah, Y. Jin, S. Kim, and K. Yu. Optical analysis of the refractive index and birefringence of hexagonal boron nitride from the visible to near-infrared. *Opt. Lett.*, 44:3797, 2019.
- [55] Farhan Rana. Lecture notes for ECE 4070, September 2016.
- [56] Farhan Rana. Lecture notes for ECE 3150, February 2017.
- [57] Farhan Rana, Okan Koksal, Minwoo Jung, Gennady Shvets, and Christina Manolatu. Many-body theory of radiative lifetimes of exciton-trion superposition states in doped two-dimensional materials. *Phys. Rev. B*, 103:035424, Jan 2021.
- [58] Farhan Rana, Okan Koksal, Minwoo Jung, Gennady Shvets, A. Nick Vamvakas, and Christina Manolatu. Exciton-trion polaritons in doped two-dimensional semiconductors. *Phys. Rev. Lett.*, 126:127402, Mar 2021.
- [59] R. Rapaport, E. Cohen, A. Ron, E. Linder, and L. N. Pfeiffer. Negatively charged polaritons in a semiconductor microcavity. *Phys. Rev. B*, 63(235310):235310, 2001.
- [60] Richard Schmidt, Tilman Enss, Ville Pietilä, Eugene Demler. Fermi polarons in two dimensions. *Phys. Rev. A*, 85:021602, 2012.
- [61] L. V. Rodriguez-de Marcos, J. I. Larruquert, J. A. Méndez, and J. A. Aznárez. Self-consistent optical constants of SiO_2 and TiO_2 films. *Opt. Mater. Express*, 6(11):3622, 2016.
- [62] Shrawan Roy, Anir S. Sharbirin, Yongjun Lee, Won Bin Kim, Tae Soo Kim, Kiwon Cho, Kibum Kang, Hyun Suk Jung, and Jeongyong Kim. Measurement of quantum yields of monolayer tmds using dye-dispersed pmma thin films. *Nanomaterials*, 10(6):1032, May 2020.
- [63] S. Barja, S. Refaely-Abramson, B. Schuler, D. Y. Qiu, A. Pulkin, S. Wickenburg, H. Ryu, M. M., Ugeda, C. Kastl, C. Chen, C. Hwang, A. Schwartzberg,

- S. Aloni, S. Mo, D. F. Ogletree, M. F. Crommie, O. V. Yazyev, S. G. Louie, J. B. Neaton, A. Weber-Bargioni. Identifying substitutional oxygen as a prolific point defect in monolayer transition metal dichalcogenides. *Nat. Commun.*, 10:3382, 2019.
- [64] S. Dhara, C. Chakraborty, K. M. Goodfellow, L. Qiu, T. A. O’Loughlin, G. W. Wicks, Subhro Bhattacharjee, A. N. Vamivakas. Anomalous dispersion microcavity trion-polaritons. *Nat. Phys.*, 14:130, 2017.
- [65] D. Sanvitto, F. Pulizzi, A. Shields, P. C. M. Christiansen, S. N. Holmes, M. Y. Simmons, D. A. Ritchie, J. C. Maan, and M. Pepper. Observation of charge transport by negatively charged excitons. *Science*, 294:837, 2001.
- [66] Christian Schneider, Arash Rahimi-Iman, Na Young Kim, Julian Fischer, Ivan G. Savenko, Matthias Amthor, Matthias Lerner, Adriana Wolf, Lukas Worschech, Vladimir D. Kulakovskii, Ivan A. Shelykh, Martin Kamp, Stephan Reitzenstein, Alfred Forchel, Yoshihisa Yamamoto, and Sven Höfling. An electrically pumped polariton laser. *Nature*, 497(7449):348–352, 2013.
- [67] Shiue-Yuan Shiao, Monique Combescot, Yia-Chung Chang. Trion ground state, excited states, and absorption spectrum using electron-exciton basis. *Phys. Rev. B*, 86:115210, 2012.
- [68] Shiue-Yuan Shiao, Monique Combescot, Yia-Chung Chang. Way to observe the implausible trion-polariton. *Europhys. Lett.*, 117:57001, 2017.
- [69] Stephan Smolka, Wolf Wuester, Florian Haupt, Stefan Faelt, Werner Wegscheider, and Ataç Imamoglu. Cavity quantum electrodynamics with many-body states of a two-dimensional electron gas. *Science*, 346(6207):332–335, 2014.
- [70] Li Bing Tan, Ovidiu Cotlet, Andrea Bergschneider, Richard Schmidt, Patrick Back, Yuya Shimazaki, Martin Kroner, and Ata ç İmamoğlu. Interacting polaron-polaritons. *Phys. Rev. X*, 10:021011, Apr 2020.
- [71] Cheng-Jyun Wang, Hsin-Chiang You, and Yu-Hsien Lin. Facile oxygen-plasma approach for depositing silicon/nitride oxide on transparent, flexible zinc-oxide thin film transistors. In *2014 21st International Workshop on Active-Matrix Flatpanel Displays and Devices (AM-FPD)*, pages 109–112, 2014.
- [72] Haining Wang, Changjian Zhang, and Farhan Rana. Ultrafast dynamics

of defect-assisted electron-hole recombination in monolayer MoS₂. *Nano Letters*, 15(1):339–345, 2015. PMID: 25546602.

- [73] L. Wang, I. Meric, P. Y. Huang, Q. Gao, Y. Gao, H. Tran, T. Taniguchi, K. Watanabe, L. M. Campos, D. A. Muller, J. Guo, P. Kim, J. Hone, K. L. Shepard, and C. R. Dean. One-dimensional electrical contact to a two-dimensional material. *Science*, 342(6158):614–617, 2013.
- [74] X. Wang, M. Zhao, and D. D Nolte. Optical contrast and clarity of graphene on an arbitrary substrate. *Appl. Phys. Lett.*, 95:081102, 2009.
- [75] C. Weisbuch, M. Nishioka, A. Ishikawa, and Y. Arakawa. Observation of the coupled exciton-photon mode splitting in a semiconductor quantum microcavity. *Phys. Rev. Lett.*, 69:3314–3317, 1992.
- [76] Y. Jin, D. H. Keum, S.J. An, J. Kim, H. S. Lee, and Y. H. Lee. A facile and efficient dry transfer technique for two-dimensional van der Waals heterostructure. *Adv. Mater.*, 27:5534, 2015.
- [77] Y. Pan, S. Li, M. Ye, R. Quhe, Z. Song, Y. Wang, J. Zheng, F. Pan, W. Guo, J. Yang, and J. Lu. Interfacial properties of monolayer MoSe₂-metal contacts. *J. Phys. Chem. C*, 120:13063, 2016.
- [78] Yifei Li, Alexey Chernikov, Xian Zhang, Albert Rigosi, Heather M. Hill, Arend M. van der Zande, Daniel A. Chenet, En-Min Shih, James Hone, Tony F. Heinz. Measurement of the optical dielectric function of monolayer transition-metal dichalcogenides: MoS₂, MoSe₂, WS₂, WSe₂. *Phys. Rev. B*, 90:205422, 2014.
- [79] Yong-Jiu Zhao, Ke-Li Wu, and Kwok-Keung M. Cheng. A compact 2-d full-wave finite-difference frequency-domain method for general guided wave structures. *IEEE Trans Microw Theory Tech*, 50:1844–1848, 2002.